

Highlights

Early and elongated epochs of planetesimal dynamo generation

Hannah R. Sanderson, James F.J. Bryson, Claire I.O. Nichols

- Thermal dynamos can begin before the dissipation of the nebula field.
- Core solidification is not required for a second epoch of dynamo generation.
- Planetesimal dynamos can last several 100 Ma longer than previously thought.
- Planetesimal radius and reference viscosity have a strong effect on dynamo duration.

Early and elongated epochs of planetesimal dynamo generation

Hannah R. Sanderson^{a,*}, James F.J. Bryson^a and Claire I.O. Nichols^a

^aDepartment of Earth Sciences, University of Oxford, South Parks Road, Oxford, OX1 3AN, UK

ARTICLE INFO

Keywords:

planetary magnetic fields
thermal evolution
meteorite magnetism
planetesimals
dynamo activity
mantle viscosity

ABSTRACT


Accreting in the first few Ma after Solar System formation, planetesimals record conditions in the protoplanetary disc and are the remnants of planetary formation processes. The meteorite paleomagnetic record carries key insights into the thermal history of planetesimals and their extent of differentiation. The current paradigm splits the paleomagnetic record into three magnetic field generation epochs: an early nebula field (<5 Ma after CAI formation), followed by thermal dynamos (5–34 Ma after CAI formation), then a gap in dynamo generation, before the onset of core solidification and compositional dynamos. The split between these epochs has been defined using current thermal evolution and dynamo generation models of planetesimals. Here we demonstrate these epochs are not as distinct as previously thought based on refined thermal evolution models that include more realistic parametrisations for mantle convection, non-eutectic core solidification and radiogenic ⁶⁰Fe in the core. We find thermal dynamos start earlier and last longer. Inclusion of ⁶⁰Fe in the core brings forward the onset of dynamo generation to 1–2 Ma after CAI formation, which overlaps with the existence of the nebula field. The second epoch of dynamo generation begins prior to the onset of core solidification, suggesting this epoch is not purely compositionally driven. Planetesimal radius is the dominant control on dynamo generation, and the choice of reference viscosity can widen the gap between epochs of dynamo generation from 0–200 Ma. Overall, timings of different planetesimal magnetic field generation mechanisms are more variable. This alters the information we can glean from the meteorite paleomagnetic record about the early Solar System. Evidence for the nebula field requires more careful interpretation and young paleomagnetic remanences, for example in the pallasites, may not be evidence for planetesimal core solidification.

1. Introduction

The strength and duration of magnetic fields generated within planetesimals can provide unique insight into the differentiation and thermal histories of rocky bodies in the early Solar System. For a rocky body to internally generate a magnetic field (a dynamo), it must have a partially molten metallic core in which flow is being driven, for example by convection. Magnetic remanences recorded by meteorites indicate that some planetesimals met these criteria during their thermal history, providing evidence for planetesimal differentiation and vigorous core flows.

Three strands of investigation can be combined to allow magnetic field generation in planetesimals to unlock planetesimal behaviour. Magnetic remanences have provided evidence for dynamos on specific parent bodies and radiometric dating of these meteorites provide estimates for the age of dynamo activity (e.g. Maurel et al., 2020). Thermal evolution models can be used to explore parent body properties, such as radius and accretion time, for which the requirements for magnetic field generation are met (e.g. Dodds et al., 2021). For undated magnetic remanences, thermal evolution models can provide possible dynamo timing constraints, for example based on the timing of core crystallisation (e.g. Tarduno et al., 2012; Bryson et al., 2015; Maurel et al., 2020; Nichols et al., 2021). Finally, thermal

*Corresponding author

 hannah.sanderson@earth.ox.ac.uk (H.R. Sanderson)

ORCID(s): 0000-0001-5842-6985 (H.R. Sanderson); 0000-0002-5675-8545 (J.F.J. Bryson); 0000-0003-2947-5694 (C.I.O. Nichols)

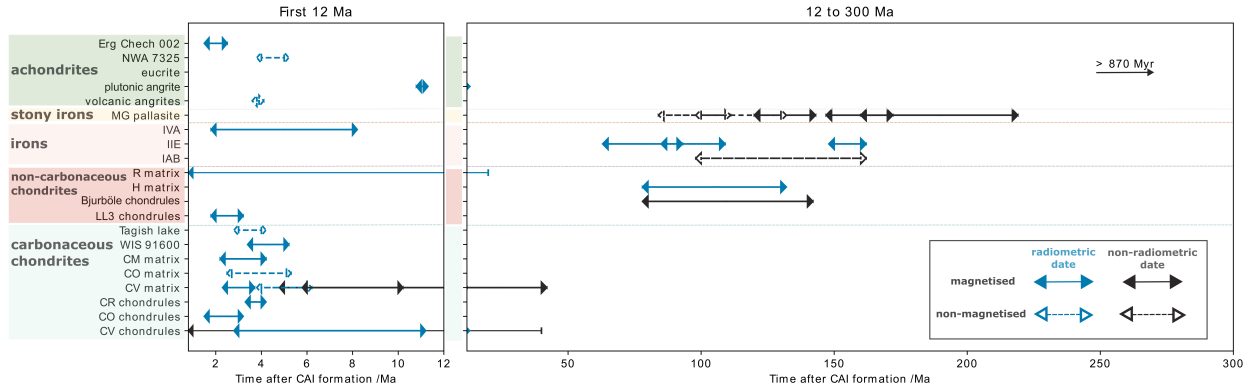


Figure 1: The meteorite paleomagnetic record. Blue and red boxes indicate undifferentiated (chondritic) meteorite groups and green, yellow and pink boxes are for differentiated (achondritic) meteorite groups. Blue and black arrows represent magnetic remanences dated using radiometric methods and thermal evolution models respectively. Solid arrows with filled caps indicate magnetised samples and dashed arrows with unfilled caps indicate unmagnetised samples. For the angrites, the time range is so short that only the arrowheads are visible. Multiple measurements for the same meteorite group are combined, but measurements of bulk magnetisation vs chondrules are kept separate to distinguish between pre-accretionary and post-accretionary remanences. Unlike the other chondrules, the CV chondrules remanence is not pre-accretionary, because the CV chondrules have experienced aqueous alteration, thermal metamorphism and possibly brecciation (Fu et al., 2014a; Shah et al., 2017). The data table shown in this plot and references for each measurement can be found in the Supplementary Materials.

evolution models can also predict whether a remanence is likely to have a dynamo or solar nebula origin (e.g. Bryson et al., 2019a; Dodds et al., 2021). Thermal evolution models to date include incomplete physical descriptions of planetesimals. Here, we use refined thermal models to re-evaluate the meteorite paleomagnetic record.

1.1. Paleomagnetic record

Meteorites with similar isotopic compositions are assumed to come from the same parent body and form a group. Paleomagnetic measurements have been recovered from both differentiated (achondritic) and undifferentiated (chondritic) meteorites from both the outer (carbonaceous) and inner (non-carbonaceous) Solar System (Figure 1).

Three possible sources have been proposed for these magnetisations: the nebula field in the protoplanetary disc, which existed prior to 5 Ma after calcium-aluminium-rich inclusion (CAI) formation (e.g. Fu et al., 2014a; Wang et al., 2017; Fu et al., 2020; Borlina et al., 2021; Bryson et al., 2023; Maurel and Gattacceca, 2024), internally generated dynamos (e.g. Tarduno et al., 2012; Wang et al., 2017; Bryson et al., 2019b) and the solar wind (Tarduno et al., 2017; O'Brien et al., 2020). Magnetisation from the solar wind is three to four orders of magnitude too weak to explain meteorite paleomagnetic remanences (Oran et al., 2018). Remanences from the nebula field can be identified by randomly oriented chondrule magnetisation directions (e.g. Fu et al., 2020).

Paleomagnetic remanences can be dated radiometrically if the closure temperature of the radiometric system is close to the blocking temperature of the magnetised mineral. Remanences dated to < 4 Ma after CAI formation have been interpreted to have a nebula origin due to the delay in the onset of dynamo generation predicted by previous

dynamo models (Dodds et al., 2021). Meanwhile, remanences younger than the dissipation of the nebula field ~ 5 Ma after CAI formation (Weiss et al., 2021) are thought to originate from planetesimal dynamos. For systems where radiometric dating is not possible or extrapolation from a dated closure temperature to the Curie temperature is required, thermal evolution models can be used to predict the timing of dynamo generation. For example, this method was used to estimate an age for the Main Group pallasite remanent magnetisation based on the timing of core crystallisation (Tarduno et al., 2012).

1.2. Thermal evolution models

Two mechanisms of dynamo generation are considered by thermal models: thermal dynamos, where temperature-induced density differences drive core convection; and compositional dynamos where density differences between solidifying pure iron and the liquid core enriched in light elements drive convection. For thermal dynamos, the superadiabatic portion of the core-mantle boundary (CMB) heat flux determines the timing and strength of magnetic field generation. Modelling compositional dynamos requires assumptions regarding the mechanism of planetesimal core solidification. The lower pressures at their CMB compared to planets mean planetesimal cores solidify inwards rather than nucleation occurring at the centre of the core (Williams, 2009). Several mechanisms for inward core solidification have been proposed, including iron snow where solid iron particles form at the CMB and then fall to the centre of the core triggering convection (Rückriemen et al., 2015; Scheinberg et al., 2016) and delamination of large iron diapirs from the CMB (Neufeld et al., 2019). Due to the complexity of these mechanisms, previous thermal evolution models of mantled planetesimals either ended after the cessation of mantle convection but prior to core solidification (Sternborg and Crowley, 2012; Dodds et al., 2021) or used the duration of eutectic core solidification as a first estimate of the timings of compositional dynamo duration (Bryson et al., 2019a; Nichols et al., 2021). Models of outward non-eutectic core solidification have been attempted but either did not model the full history of the body, or only considered cooling by mantle conduction (Nimmo, 2009; Bryson et al., 2015; Nichols et al., 2021).

Previous thermal evolution models (e.g. Sternborg and Crowley, 2012; Bryson et al., 2019a; Dodds et al., 2021) that successfully generate dynamos predict several events in the thermal evolution.

- (i) Following instantaneous or during gradual accretion, planetesimals are heated by ^{26}Al decay, causing the body to differentiate into a metallic core and silicate mantle.
- (ii) Following differentiation, ^{26}Al preferentially partitions into the silicate mantle. After further heating, the melt fraction in the mantle is high enough to initiate mantle convection. The core is heated by the mantle from above and develops a stable thermal stratification which prevents the onset of a dynamo.
- (iii) Once the mantle cools below the temperature at the CMB, the core thermal stratification is removed and the CMB heat flux becomes superadiabatic. Core convection triggers the onset of thermal dynamo generation.

- (iv) As the mantle cools, it becomes more viscous until mantle convection ceases. The cessation of mantle convection leads to a sharp decrease in CMB heat flux and core convection drops below the critical value, terminating the dynamo.
- (v) Eventually the core cools below its solidus temperature and begins to solidify, which can lead to a compositional dynamo and a second epoch of dynamo generation.
- (vi) Once the core has fully solidified, dynamo generation is no longer possible.

These previous models predict two epochs of dynamo generation: an early thermal dynamo and a second later compositional dynamo during core solidification. This has led to paleomagnetic remanences > 65 Ma after CAI formation being interpreted as evidence of a solidifying core (Bryson et al., 2015; Nichols et al., 2016, 2021; Maurel et al., 2021) and remanences < 4 Ma after CAI formation being interpreted as a record of a nebula field due to the delay in start time of thermal dynamos caused by core thermal stratification (Bryson et al., 2019a, 2020a; Fu et al., 2021).

These earlier models assumed certain values or omitted processes that are re-explored here. First, they neglect heating from ^{60}Fe in the core, because for low values of primordial $^{60}\text{Fe}/^{56}\text{Fe}=10^{-8}$ (such as measured by Tang and Dauphas, 2012), it only leads to a 10 K difference in core temperature over the lifetime of the planetesimal (Henke et al., 2013). However, new measurements suggest $^{60}\text{Fe}/^{56}\text{Fe}$ may have been as high as $6 \pm 2 \times 10^{-7}$ in the formation region of carbonaceous chondrites (Cook et al., 2021). Therefore, the role ^{60}Fe on planetesimal core thermal evolution should be explored for a wider range of values.

Second, previous thermal evolution models do not fully combine thermal and compositional dynamo generation, mantle convection and non-eutectic core solidification. This limits the ability of existing thermal evolution models to predict the full magnetic history of a body.

Third, the effect of mantle viscosity on magnetic field generation has not been investigated in previous thermal models. CMB heat flux is limited by the cooling rate of the mantle above and the thickness of the CMB boundary layer, which are both governed by the mantle viscosity. Therefore, the parameterisation of mantle viscosity as a function of temperature has a critical role in planetesimal thermal evolution.

Sanderson et al. (2024) describe the implementation of a new model, which that accounts for all the points discussed above. Here, this new model is applied across the full range of realistic parameters to reassess the existing meteorite paleomagnetic record.

2. Methods

This study uses the Sanderson et al. (2024) 1D spherically symmetric planetesimal thermal evolution model combined with dynamo scaling laws to predict the timings of dynamo generation in planetesimals with a radius up to 500 km. This model builds on the previous planetesimal thermal evolution models of Sterenborg and Crowley

(2012), Bryson et al. (2019a) and Dodds et al. (2021) by including radiogenic heating from ^{60}Fe in the core, an adjustable mantle viscosity law, and updated stagnant lid and CMB boundary layer parametrisations that better reflect mantle conditions. The model includes both convection and conduction in the mantle and models magnetic field generation by non-eutectic core solidification. The details and complete mathematical description of this model can be found in Sanderson et al. (2024).

2.1. Thermal evolution model

All model runs begin at 0.8 Ma after CAI formation with instantaneous accretion of the body at 200 K. The body heats up due to radiogenic heating of ^{26}Al and the Fe-FeS and silicate phases melt until the silicate reaches its critical melt fraction, ϕ_C . At this point, differentiation is assumed to take place instantaneously, as the molten, dense Fe-FeS sinks through the rheologically weak silicates to the centre. The model then consists of two coupled reservoirs: the Fe-FeS core and the silicate mantle. The surface temperature is held constant at 200 K throughout the simulation.

In the mantle, heat is transported either by conduction or convection. Mantle convection is assumed to occur in the stagnant lid regime with an isothermal, convective layer between conductive boundary layers at the CMB and the surface. These boundary layers thicken as the mantle cools and convection ceases once the combined CMB and surface boundary layer thicknesses exceed the total mantle thickness. The temperature at the CMB is calculated by assuming continuity of heat flux across the boundary.

The core also transports heat by conduction or convection. For the core to convect either the CMB heat flux, F_{CMB} , must be superadiabatic or the core must be solidifying (not at the eutectic). During core solidification, the density difference between the more dense, solidified pure iron and the less dense Fe-FeS liquid drives core convection, as the solidified iron sinks to the centre of the core. When the core is convecting, the combined thermal and compositional buoyancy flux can be used to calculate a magnetic field strength (see Sanderson et al., 2024, for details). Once the eutectic composition is reached, core solidification no longer generates a compositional buoyancy flux. Combining buoyancy flux contributions enables the thermal and compositional drivers of convection to be considered simultaneously. The model ends once the whole core has solidified and dynamo generation is no longer possible.

2.1.1. Dynamo generation

The vigour of convection in the liquid part of the core is characterised by the magnetic Reynolds number, Re_m , which must be supercritical for the core flow to be strong enough to generate a magnetic field. The analytical estimate of the critical value is 10, while from empirical simulations it ranges from 40–100 (Stevenson, 2003; Aubert et al., 2009). We use a critical Re_m of 10 in line with previous work (Bryson et al., 2019a; Dodds et al., 2021). However, the proportions of model runs with $10 \leq Re_m < 40$, $40 \leq Re_m < 100$ and $Re_m \geq 100$ are also investigated.

2.2. Parameter variation

Models were run for a range of mantle viscosities, planetesimal radii, initial core sulfur contents, $X_{S,0}$, and $^{60}\text{Fe}/^{56}\text{Fe}$ ratios in the accreted material (Table 1).

The temperature dependence of mantle viscosity is defined piece-wise (Figure 2) by five control parameters. Below the solidus, the viscosity has an Arrhenius temperature dependence with slope β , which is proportional to the activation energy for viscous deformation. At the solidus, the mantle has a reference viscosity, η_0 . Above the solidus, melt weakens the material and the viscosity decreases with a steeper Arrhenius dependence, quantified by the melt weakening exponent, α_n (Hirth and Kohlstedt, 2003). At the critical melt fraction, ϕ_C , there is enough melt to completely surround any remaining solid phases and the material disaggregates with a rapid drop in viscosity. Beyond ϕ_C , the viscosity tends to a constant liquid viscosity, η_l , following the Krieger-Dougherty relation (Sturtz et al., 2022) as the melt fraction tends to one.

Each parameter was varied independently while the others were held constant at the median value of their range. The justifications for each parameter range are detailed in the following subsections.

2.2.1. Reference viscosity, η_0

The reference viscosity, η_0 , ranges from 10^{14} – 10^{24} Pas. The lower bound is based on experimental measurements (Scott and Kohlstedt, 2006) while the upper bound is set by extrapolating reference viscosities used in models of Ganymede (Rückriemen et al., 2018) to planetesimal mid-mantle pressures (see Appendix A).

2.2.2. Critical melt fraction, ϕ_C

Experiments suggest the critical melt fraction, ϕ_C , is between 0.2–0.3 (Scott and Kohlstedt, 2006). However thermal evolution models of planetesimals both for dynamo generation (Sternborg and Crowley, 2012; Bryson et al., 2019a; Dodds et al., 2021), and differentiation (e.g. Lichtenberg et al., 2019; Monnereau et al., 2023) use a value of $\phi_C=0.5$. Although it is unclear if $\phi_C=0.5$ is physically reasonable, this model applied ϕ_C between 0.2–0.5 to enable comparison with previous models.

2.2.3. Arrhenius slope, β

The Arrhenius slope in the viscosity law, β , is typically defined as $\frac{E}{RT_{ref}^2}$, where E is the activation energy, $R = 8.31 \text{ J mol}^{-1} \text{ K}^{-1}$ is the gas constant and T_{ref} is a reference temperature - often taken to be the temperature at which the reference viscosity is measured. Experimentally measured activation energies for a range of silicate mantle compositions and strain rates range from 240–570 kJ mol $^{-1}$ (Karato and Wu, 1993; Hirth and Kohlstedt, 2003). For a reference temperature of the mantle solidus (1400 K), this corresponds to $\beta=0.015$ – 0.035 K^{-1} . Dodds et al. (2021) used $\beta = 0.01 \text{ K}^{-1}$ so to enable comparison with previous thermal evolution models. Here we explore $\beta = 0.01$ – 0.035 K^{-1} .

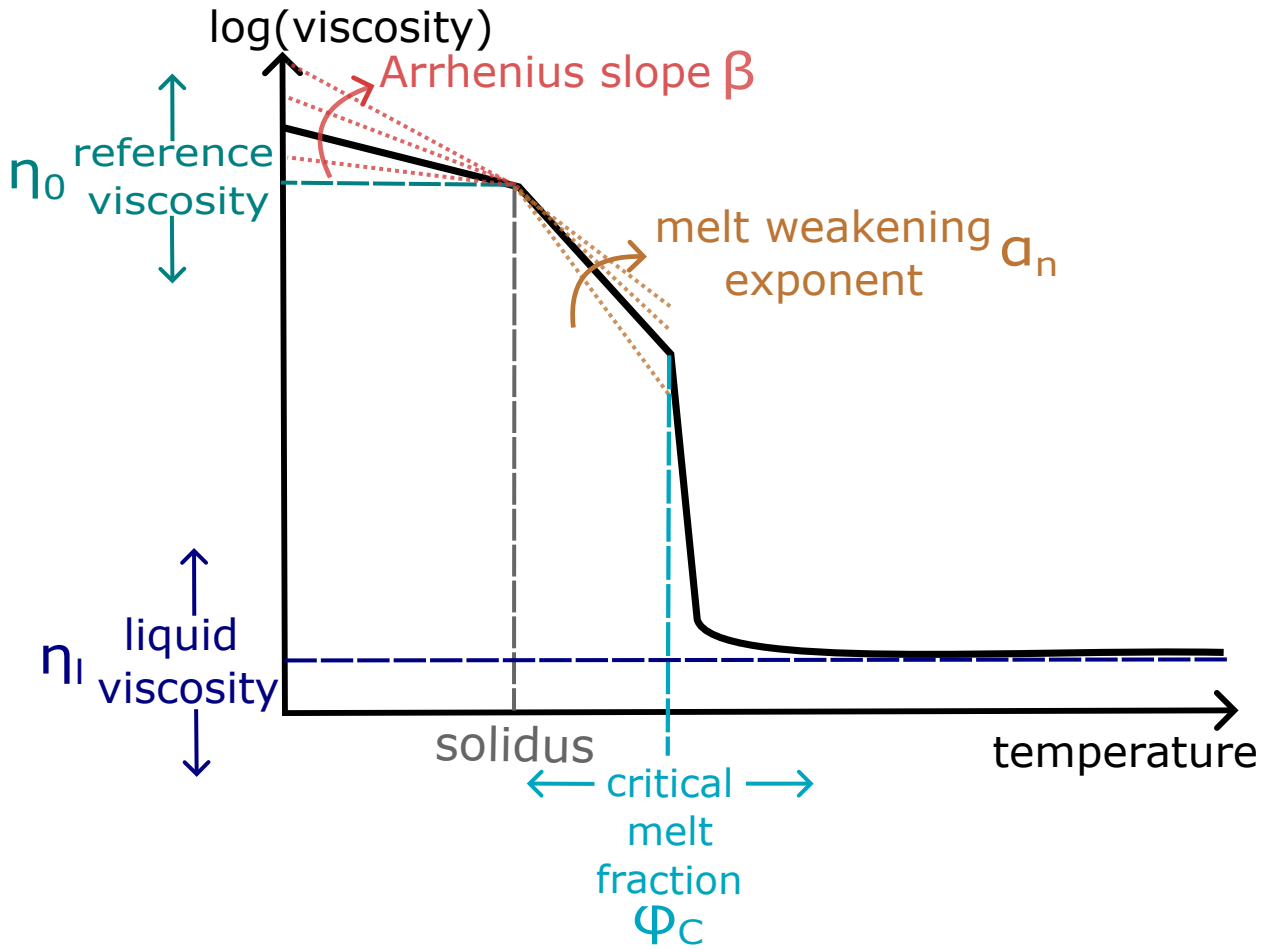


Figure 2: Illustration of parameters varied in the mantle viscosity model. Reference viscosity, $\eta_0=10^{14}\text{--}10^{24}$ Pas, is the viscosity at the mantle solidus. Liquid viscosity, $\eta_l=1\text{--}100$ Pas, is the viscosity when the mantle is fully molten. Critical melt fraction, $\phi_c=0.2\text{--}0.5$, is the melt fraction for which all crystals become surrounded by melt, the material disaggregates and becomes rheologically weak. Arrhenius slope, $\beta=0.01\text{--}0.035\text{ K}^{-1}$, determines the rate of decrease in viscosity with increasing temperature. Melt weakening exponent, $\alpha_n=25\text{--}40$, determines the additional rate of decrease in viscosity with increasing temperature due to melting.

2.2.4. Melt weakening exponent, α_n

The melt weakening exponent, α_n , depends on whether deformation occurs by diffusion creep ($\alpha_n=25\text{--}30$) or dislocation creep ($\alpha_n=30\text{--}45$) (Hirth and Kohlstedt, 2003). To cover both deformation modes this model investigated values from 25–45.

2.2.5. Liquid viscosity, η_l

The liquid viscosity, η_l , is determined by mantle composition and can range from 1–100 Pas across the compositions of all volcanic rocks commonly encountered on Earth (Giordano et al., 2008). Increasing silica content increases viscosity and increasing volatile content decreases viscosity (Leshner and Spera, 2015).

Symbol	Meaning	Range of values	Constant value	Reference
η_0	Reference viscosity	10^{14} – 10^{24} Pas	10^{19} Pas	a, b
ϕ_C	Critical melt fraction	0.2–0.5	0.3	a, c
β	Arrhenius slope	0.01 – $0.035 K^{-1}$	$0.0225 K^{-1}$	a, d, e
α_n	Melt weakening exponent	25–45	30	f
η_l	Liquid viscosity	1–100 Pas	10 Pas	g
$X_{S,0}$	Initial core sulfur content	26.7–33 wt%	29.85 wt%	h, i, j, k
$^{60}\text{Fe}/^{56}\text{Fe}$	$^{60}\text{Fe}/^{56}\text{Fe}$ in accreting material	0 – 6×10^{-7}	10^{-8}	
r	Planetesimal Radius	100–500 km	300 km	

Table 1

Values for variable and constant parameters in simulations as described in Section 2.2. The upper five parameters occur in the viscosity law. The range on $X_{S,0}$ is for a 300 km radius planetesimal. For [500, 400, 200, 100] km radius planetesimals the minimum and median $X_{S,0}$ were [25.9, 26.3, 27.1, 27.1] wt% and [29.45, 29.65, 30.05, 30.05] wt% respectively. (a) Scott and Kohlstedt (2006), (b) Rückriemen et al. (2018), (c) Bryson et al. (2019a), (d) Karato and Wu (1993), (e) Dodds et al. (2021), (f) Hirth and Kohlstedt (2003), (g) Giordano et al. (2008), (h) Tang and Dauphas (2012), (i) Cook et al. (2021), (j) Kodolányi et al. (2022a), (k) Kodolányi et al. (2022b).

2.2.6. Initial core sulfur content, $X_{S,0}$

The initial core sulfur content, $X_{S,0}$, ranges from the minimum Fe-FeS sulfur content for which the metal phase will be fully molten before differentiation to the eutectic (33 wt% for $T_{s,Fe} = 1260$ K for $R=300$ km). The Fe-FeS liquidus temperature is pressure dependent so the minimum Fe-FeS changes with planetesimal radius.

2.2.7. Primordial $^{60}\text{Fe}/^{56}\text{Fe}$

Estimates on the primordial $^{60}\text{Fe}/^{56}\text{Fe}$ vary by almost two orders of magnitude from 10^{-8} (e.g. Tang and Dauphas, 2012) to 6×10^{-7} (e.g. Cook et al., 2021). However, previous thermal evolution and dynamo models neglected the presence of ^{60}Fe in the core. Therefore, the model was run for five values of $^{60}\text{Fe}/^{56}\text{Fe} = [0, 1 \times 10^{-9}, 1 \times 10^{-8}, 1 \times 10^{-7}, 6 \times 10^{-7}]$ to cover the full range of possible values and compare with previous models.

2.2.8. Planetesimal radius, r

Models were run for planetesimal radii between 100–500 km. The lower limit is set by previous estimates for the minimum radius for compositional dynamo generation (Nimmo, 2009). The upper limit corresponds approximately to the radius of Ceres, the largest known asteroid today.

3. Results

3.1. Constant radius

Firstly, we ran models with a constant radius of 300 km to identify the impact of other parameters on thermal evolution and dynamo generation. The lowest mantle reference viscosities, η_0 , and initial core sulfur content, $X_{S,0}$, result in a single epoch of dynamo generation and a single value in each of η_0 , ϕ_C , and α_n result in three epochs of dynamo generation. The other parameter values have two periods of dynamo generation (Figure 3). Across these two dynamo generation periods, we observe two distinctive trends in magnetic field strength: (i) the first dynamo generation

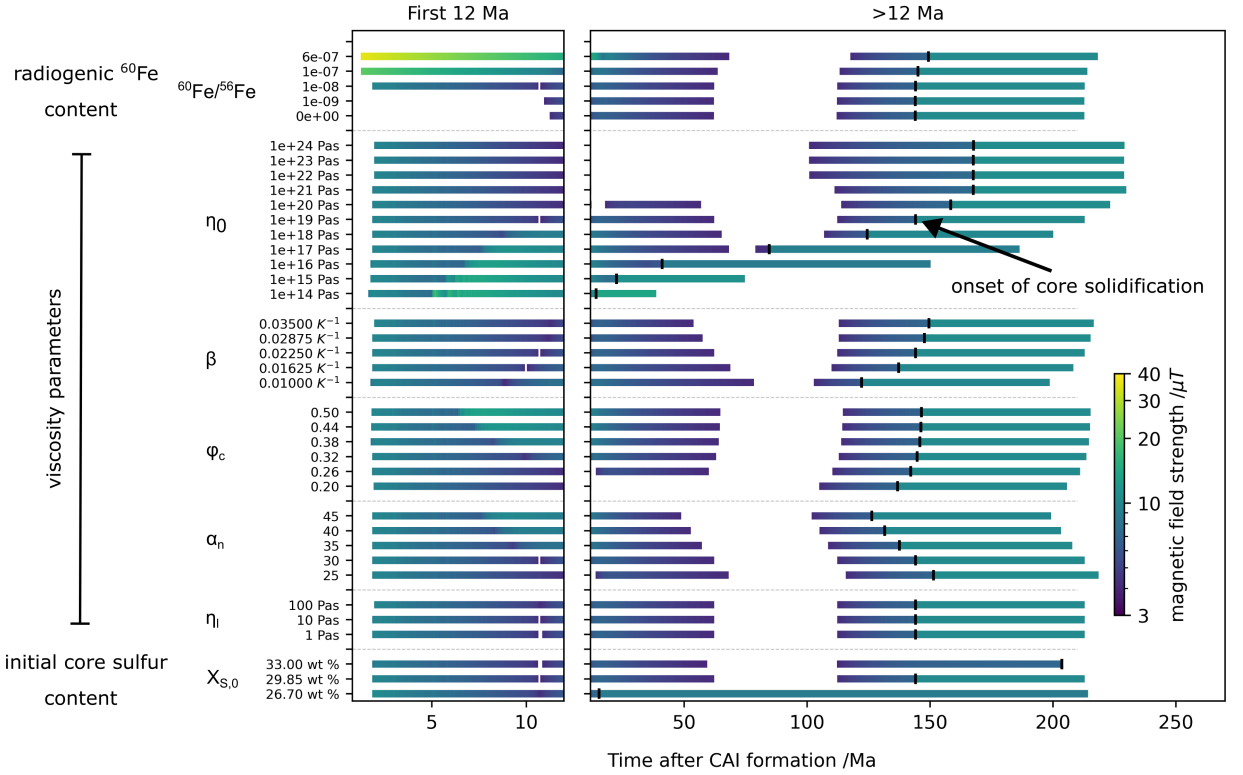


Figure 3: Dynamo timings for a 300 km planetesimal for a range of initial $^{60}\text{Fe}/^{56}\text{Fe}$, mantle viscosities and core compositions. Filled bars indicate periods when a dynamo is active and the colour of the bar indicates dipole magnetic field strength at the surface. The small, vertical, black line on each bar indicates the onset of core solidification in each model run. Magnetic field strengths between the onset of core solidification and the end of dynamo generation are averages for this time interval to remove oscillations in field strength due to the discretisation of the model (Sanderson et al., 2024). The thin, vertical, white lines in some runs are <0.5 Ma breaks in dynamo generation due to a jump in viscosity at ϕ_c and are not a significant break in dynamo generation. For each parameter, the model was run across the range of values in Table 1, while all other parameters are held at a constant median value. The constant parameter values were: $\eta_0 = 10^{19}$ Pas, $\beta = 0.0225 \text{ K}^{-1}$, $\alpha_n = 30$, $\phi_c = 0.3$, $\eta_l = 10$ Pas, $^{60}\text{Fe}/^{56}\text{Fe} = 10^{-8}$, $X_{S,0} = 29.85 \text{ wt}\%$.

period, has two peaks in magnetic field strength: one corresponds to the onset of dynamo generation and the other to when the base of the mantle first cools below the critical melt fraction (Sanderson et al., 2024), ii) in the second dynamo generation period, magnetic field strength increases with time towards a peak value during core solidification. For all runs with multiple field generation periods, the final dynamo generation period begins before the onset of core solidification. Reference viscosity has the strongest effect on the duration of the gap in dynamo generation and $^{60}\text{Fe}/^{56}\text{Fe}$ has the strongest influence on the resulting magnetic field strength. Despite the range in dynamo durations and strengths, most Re_m fall between 10–40 (Figure 4).

3.1.1. Effect of ^{60}Fe

Increasing $^{60}\text{Fe}/^{56}\text{Fe}$ brings forward the onset of the dynamo to 1–2 Ma after CAI formation and increases peak field strength and Re_m in the first epoch of dynamo generation. The onset of the dynamo is earlier for increased ^{60}Fe ,

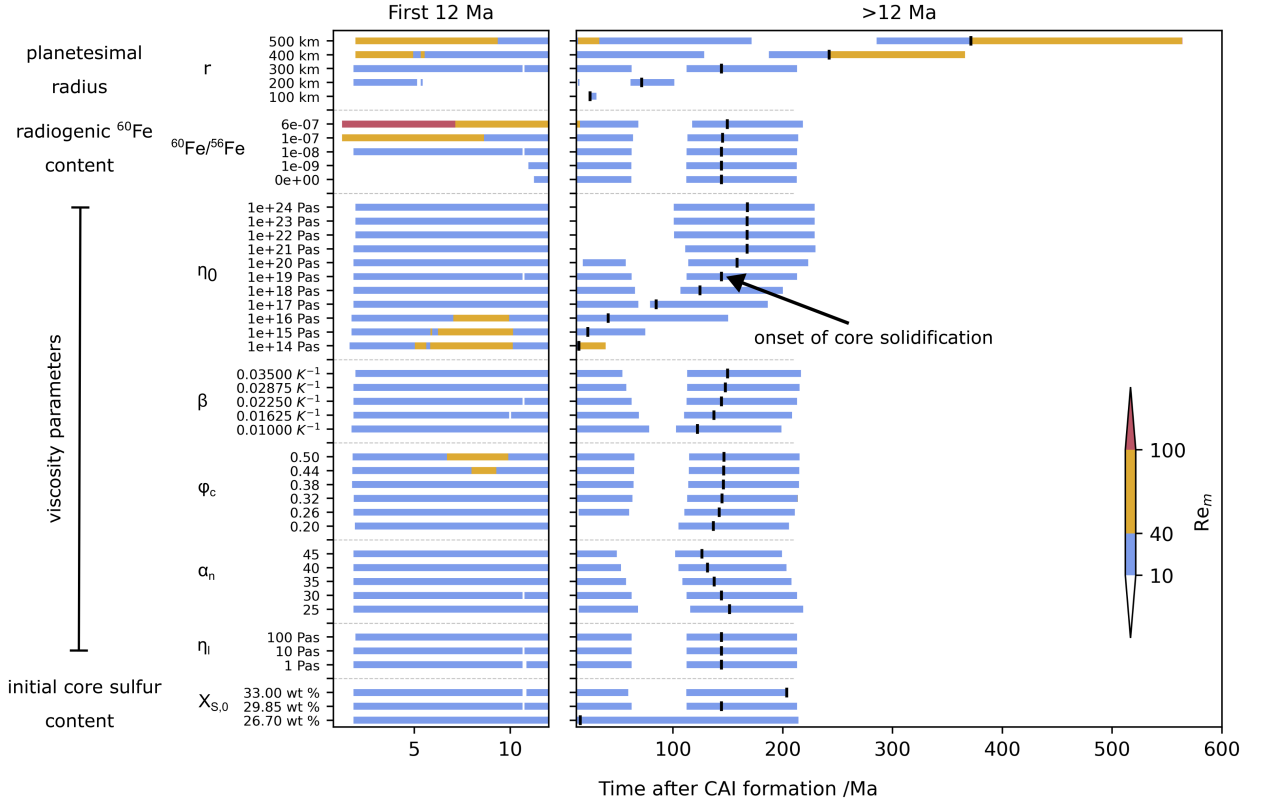


Figure 4: Magnetic Reynolds number (Re_m) as a function of time for a range of for a range of initial $^{60}\text{Fe}/^{56}\text{Fe}$, mantle viscosities, core compositions and planetesimal radii. Filled bars indicate periods when the dynamo is on and the colour of the bars indicates the magnetic Reynolds number. Subcritical values (< 10) are not shown. Supercritical values are categorised according to the range of possible criticality limits: 10-40, 40-100 and >100 (Christensen and Aubert, 2006; Stevenson, 2003). The small, vertical, black line on each bar indicates the onset of core solidification in each model run. Magnetic Reynolds numbers between the onset of core solidification and the end of dynamo generation are averages for this time interval to remove oscillations in Re_m due to the discretisation of the model (Sanderson et al., 2024). The thin, vertical, white lines in some runs are $< 0.5 Ma$ breaks in dynamo generation due to a jump in viscosity at ϕ_c and are not a significant break in dynamo generation. For each parameter, the model was run across the range of values in Table 1 and shown on Figure 3, while all other parameters were held at a constant median value. The range of values for radius are shown explicitly. The constant parameters values are: $r = 300 \text{ km}$, $\eta_0 = 10^{19} \text{ Pas}$, $\beta = 0.0225 \text{ K}^{-1}$, $\alpha_n = 30$, $\phi_c = 0.3$, $\eta_i = 10 \text{ Pas}$, $^{60}\text{Fe}/^{56}\text{Fe} = 10^{-8}$, $X_{S,0} = 29.85 \text{ wt}\%$.

because increased heating erodes core thermal stratification more rapidly or prevents its formation altogether, which brings forward the time that the CMB heat flux (F_{CMB}) becomes superadiabatic. Radiogenic heating by ^{60}Fe also increases the temperature of the core and the temperature difference relative to the mantle, which increases F_{CMB} and the strength of the dynamo. Model runs with $^{60}\text{Fe}/^{56}\text{Fe} \geq 10^{-7}$ had peak field strengths in the first period of dynamo generation 2–3 times higher than runs with $^{60}\text{Fe}/^{56}\text{Fe} = 10^{-8}$. This extra heat is removed from the core by an elevated F_{CMB} during the first period of dynamo generation so by the second epoch of dynamo generation the peak field strengths, Re_m and the onset of core solidification are similar across values of $^{60}\text{Fe}/^{56}\text{Fe}$. $^{60}\text{Fe}/^{56}\text{Fe} = 0$ and $^{60}\text{Fe}/^{56}\text{Fe} = 10^{-9}$ result in similar onset times and field strengths for the first dynamo generation period, suggesting that when

$^{60}\text{Fe}/^{56}\text{Fe} \leq 10^{-9}$ the effect of ^{60}Fe can be neglected. The onset times vary little across variations in other parameters indicating $^{60}\text{Fe}/^{56}\text{Fe}$ is the dominant control on onset time for the first period of dynamo generation.

3.1.2. *Effect of viscosity*

The reference viscosity, η_0 , has the strongest effect on the duration of the first period of dynamo generation and the following gap. Above a threshold value of 10^{21} Pas, the first period of dynamo generation ends after 13-14 Ma and there is a gap of >80 Ma in dynamo duration. This results from the rapid thickening of the surface stagnant lid shutting off convection earlier for the highest reference viscosities. In contrast, below a threshold value of 10^{16} Pas, there is only one epoch of dynamo generation, because the mantle viscosity is sufficiently low that mantle convection does not cease before core solidification. The second peak in magnetic field strength in the first epoch of dynamo generation widens and increases in strength with decreasing reference viscosity, because the thinner boundary layer at the CMB raises F_{CMB} . An elevated F_{CMB} increases the rate at which the core cools, which brings forward the onset of core solidification and the end of dynamo generation.

The second lowest value of critical melt fraction, ϕ_C , and $\eta_0 = 10^{20}$ Pas result in three epochs of field generation. The first break between field generation epochs occurs when the temperature at the base of the mantle drops below the temperature of ϕ_C . At this temperature, there is a jump in mantle viscosity and CMB boundary layer thickness which decreases F_{CMB} enough to temporarily turn off core convection (for a more detailed description of CMB boundary layer thickness with time see Sanderson et al., 2024).

The viscosity parameters have very little effect on the supercriticality of Re_m . Only the lowest η_0 and highest values of ϕ_C increase the Re_m in the first 12 Ma (Figure 4). The lowest values of η_0 are less physical, based on highest values from laboratory experiments, which have not been extrapolated to planetesimal pressure values so this increase in Re_m can be discounted. However, the highest value $\phi_C = 0.5$ is the value assumed in previous thermal evolution models and the elevated Re_m for this value may have resulted in overestimates of field strength and dynamo duration in previous work.

3.1.3. *Effect of $X_{\text{S},0}$*

Initial core sulfur content, $X_{\text{S},0}$, has a strong effect on the timing of core solidification, because increasing $X_{\text{S},0}$ lowers the liquidus temperature of the core and more cooling is required to reach this temperature. The lowest $X_{\text{S},0}$ removes the gap in dynamo generation, because the early onset of core solidification provides additional compositional buoyancy flux to drive the dynamo even when mantle convection ceases.

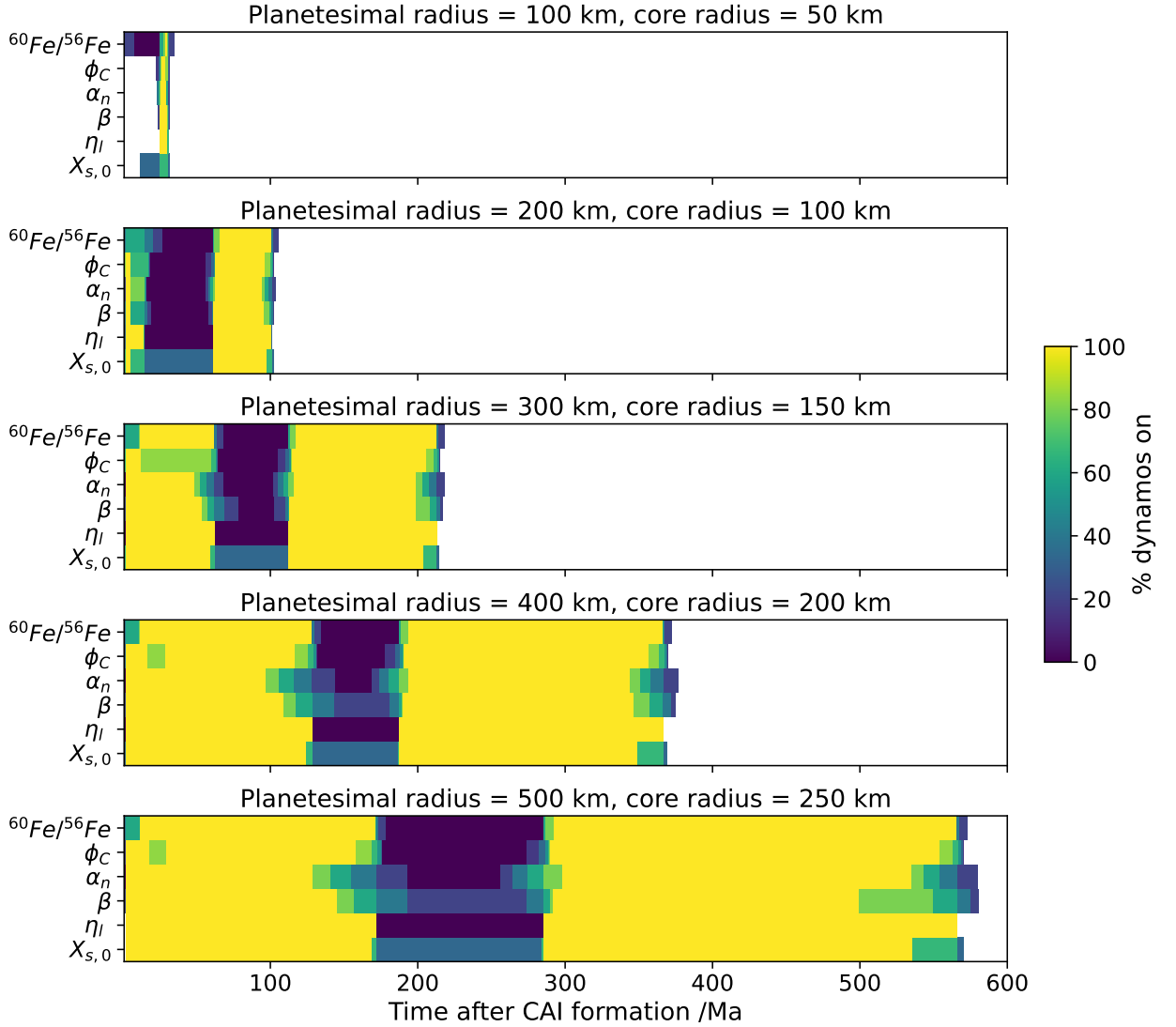


Figure 5: Proportion of active dynamos for variation in initial $^{60}\text{Fe}/^{56}\text{Fe}$, mantle viscosities and core compositions for planetesimals ranging from 100-500 km in radius. In an individual panel, model runs are grouped in horizontal blocks by parameter. Yellow indicates that all dynamos are on at a given time irrespective of the value of a parameter, dark blue indicates no dynamos are on at a given time irrespective of the value of a parameter. Light blue to green regions indicate a dynamo is on for a subset of values of that parameter. White space indicates times after the last period of dynamo generation and the end of the simulation. The constant parameters values are: $\eta_0 = 10^{19}$ Pas, $\beta = 0.0225 \text{ K}^{-1}$, $\alpha_n = 30$, $\phi_C = 0.3$, $\eta_I = 10$ Pas, $^{60}\text{Fe}/^{56}\text{Fe} = 10^{-8}$ and the range for each parameter is given in Table 1. η_0 causes a wide variation in dynamo timings, so is shown separately in Figure 6.

3.2. Variable radius

To identify the impact of planetesimal radius on thermal evolution and dynamo generation we ran models with varying radii and other variables being held constant (Table 1). Core radius was assumed to be half planetesimal radius. Planetesimal radius has the strongest effect on dynamo timing, duration, and width of the gap in dynamo generation (Figure 5). Larger planetesimals cool more slowly so mantle convection ceases later, which prolongs the

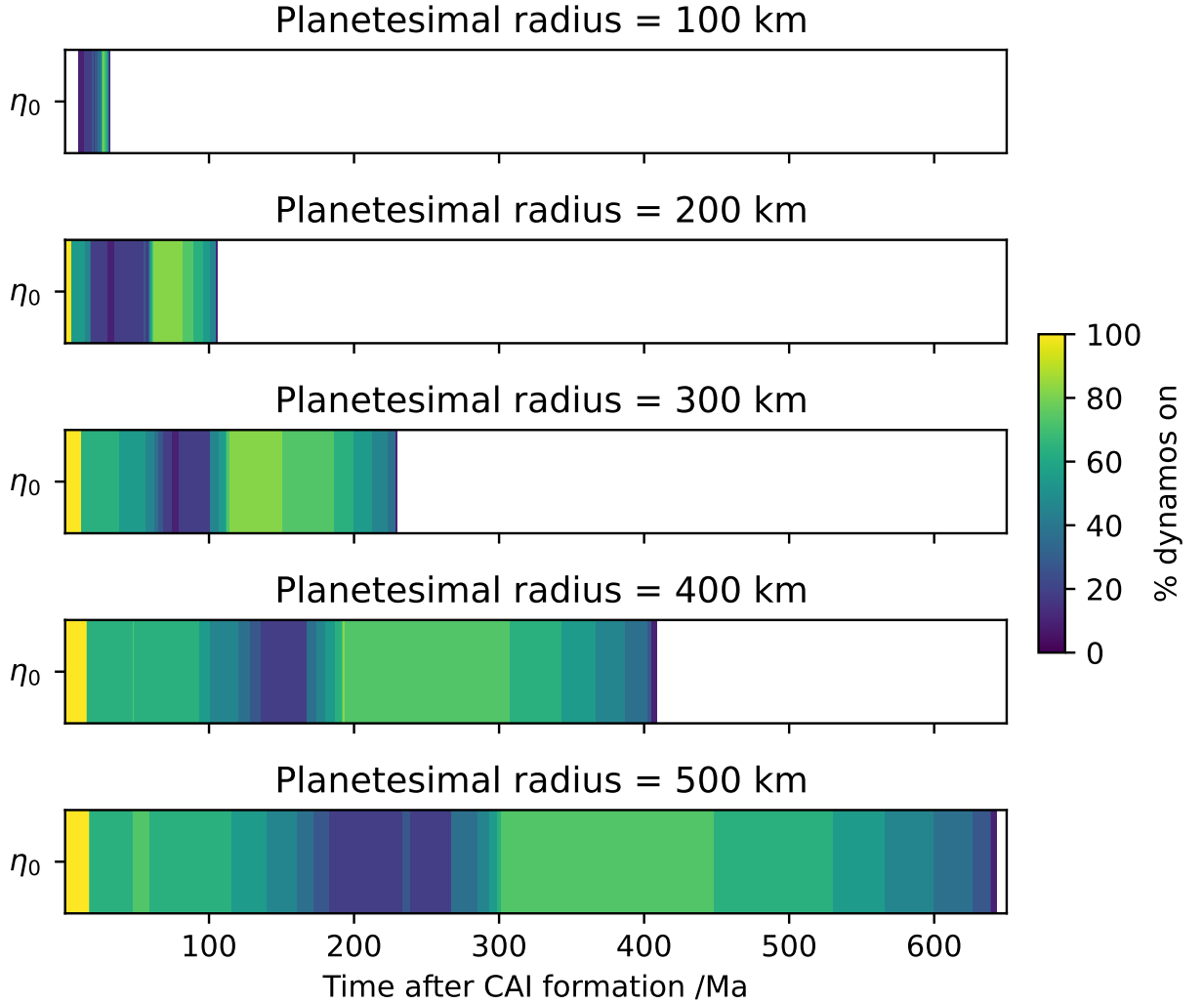


Figure 6: Proportion of active dynamos across a range of reference viscosity, η_0 , for planetesimals ranging from 100–500 km in radius. Core radius is half planetesimal radius. Yellow indicates that all dynamos are on at a given time irrespective of the value of η_0 , dark blue indicates no dynamos are on at a given time irrespective of the value of η_0 . Light blue to green regions indicate a dynamo is on for a subset of values of η_0 . White space indicates times after the last period of dynamo generation and the end of the simulation. The constant parameter values are: $\beta = 0.0225 \text{ K}^{-1}$, $\alpha_n = 30$, $\phi_C = 0.3$, $\eta_l = 10 \text{ Pas}$, $^{60}\text{Fe}/^{56}\text{Fe} = 10^{-8}$, $X_{S,0} = [29.45, 29.65, 29.85, 30.05, 30.05] \text{ wt\%}$ for [500, 400, 300, 200, 100] km radius planetesimals. The range for η_0 is given in Table 1.

first epoch of dynamo generation. Larger core size increases the lengthscale of convection; this raises the Re_m for a given F_{CMB} , which further prolongs dynamo generation. Larger core size also increases magnetic field strengths (Figure S1–S4). The magnetic increase in field strength is most pronounced at the onset of the first epoch of dynamo generation for the highest values of $^{60}\text{Fe}/^{56}\text{Fe}$. Bodies with radius of 100 km only generate magnetic fields after the onset of core solidification (Figure 4) except for the highest values of $^{60}\text{Fe}/^{56}\text{Fe}$. Increasing planetesimal radius from 100 km to 500 km increases the end time of dynamo generation from ~ 30 to ~ 600 Ma. The gap in dynamo generation

moves later and increases in duration for increasing planetesimal radius. For each body size, the timings of the dynamo generation periods are consistent across variations in the other parameters (Figure 5). The duration of the gap in dynamo generation varies slightly, but the gap occurs in the same place across variations in a parameter. An exception is η_0 (Figure 6), where values $<10^{16}$ Pas do not produce a gap in dynamo generation. However, for η_0 there is still a trend of increasing dynamo duration with radius.

4. Discussion

4.1. Reevaluating the paleomagnetic record

We predict a wider range of timings of planetesimal dynamo generation than previous models. Inclusion of ^{60}Fe can bring forward the onset of thermal dynamos to 1–2 Ma after CAI formation, which allows for dynamo generation prior to the dissipation of the nebula field (Figure 7). The overlap of thermal dynamos with the nebula field means paleomagnetic remanences previously attributed to the nebula field should be re-evaluated. The first epoch of dynamo generation can last until 20–200 Ma after CAI formation (depending on radius) rather than until 9–34 Ma after CAI formation suggested by previous models (Dodds et al., 2021). The second epoch of dynamo generation begins before the onset of core solidification. Therefore, magnetic remanences previously attributed to the second epoch of dynamo generation during core solidification may not have been in the second epoch and do not require core solidification. The meteorite paleomagnetic record in light of our new model results is reassessed below.

4.1.1. Paleomagnetic records of the nebula field

Unidirectional magnetisation within chondrules, but non-unidirectional magnetisation between chondrules can provide paleointensities of the nebula field. CO (Borlina et al., 2021), LL3 (Fu et al., 2014b) and CR chondrule (Fu et al., 2020) measurements have been interpreted as evidence for a nebula field 1.7–4 Ma after CAI formation with paleointensities up to $150\mu\text{T}$ (Figure 7). Magnetisation in the ungrouped achondrite Erg Chech 002 from 2 ± 0.3 Ma after CAI formation has also been interpreted as evidence for the nebula field (Maurel and Gattacceca, 2024), because the Erg Chech parent body is believed to have been too small to generate a dynamo (Neumann et al., 2023).

Measurements of volcanic angrites, which do not record a remanence 3.8–3.9 Ma after CAI formation¹ have been interpreted as evidence for the end of the nebula field in the inner Solar System (Wang et al., 2017). An upper limit on paleointensity of $0.6\mu\text{T}$ from NWA 7325 4–5 Ma after CAIs (Weiss et al., 2017) further supports that the nebula field in the inner Solar System had dissipated by this time. Upper limits on paleointensity of $0.9\mu\text{T}$ from the matrix of CO chondrites (Borlina et al., 2022) and no high temperature remanence in the CV chondrite Kaba (Gattacceca et al., 2016) is also consistent with the dissipation of the nebula field in the outer Solar System 3–5 Ma after CAI formation.

¹These ages were originally reported as absolute Pb-Pb ages and may be shifted to 4.8–4.9 Ma after CAI formation based on reevaluation of the anchor for Pb-Pb (Piralla et al., 2023).

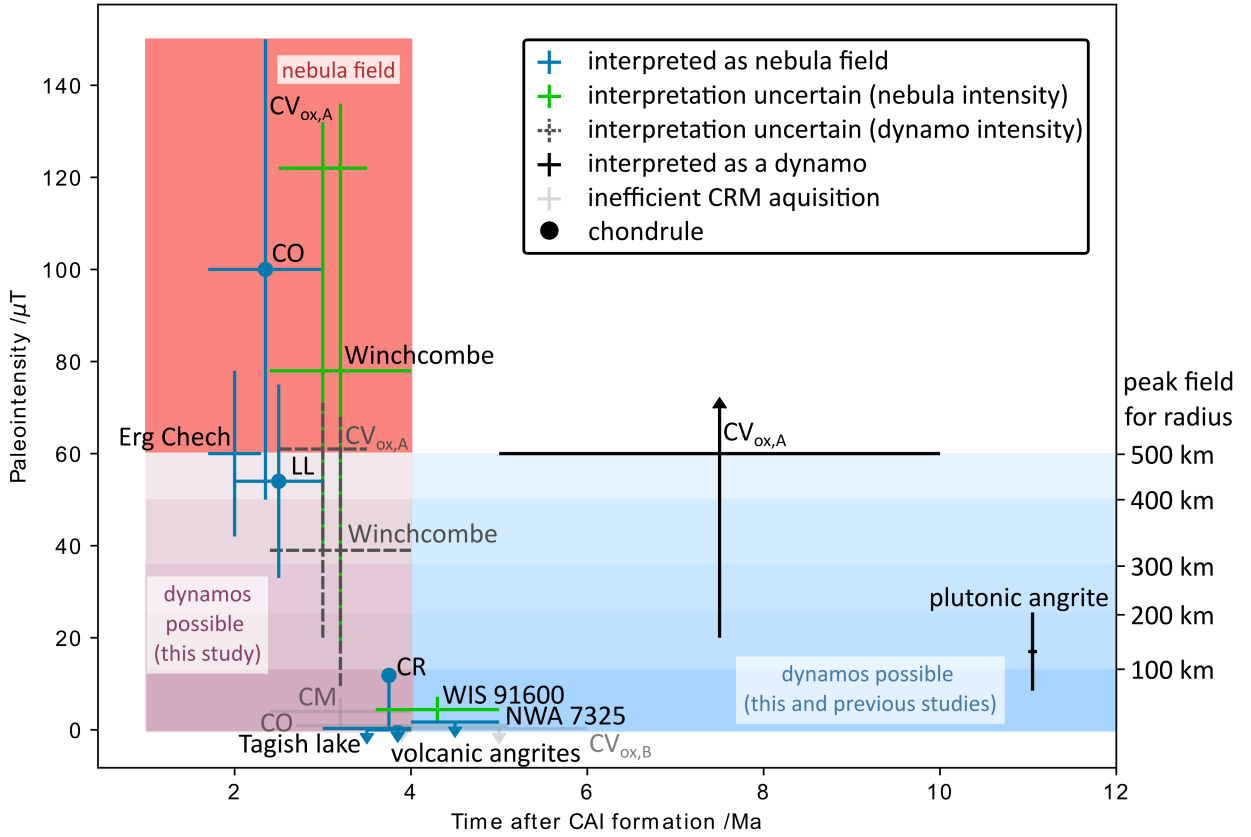


Figure 7: A summary of meteorite paleointensities for the first 12 Ma after CAI formation. Meteorites for which the cause of magnetisation is interpreted as a nebula field (or lack of) are plotted in blue. Meteorites for which the cause of magnetisation has been interpreted as a dynamo field are plotted in black. Meteorites which could have a nebula or dynamo origin are plotted in green for their possible nebula field paleointensities and the dashed grey lines indicate the paleointensities of Winchcombe (Bryson et al., 2023) and Allende (Fu et al., 2021) if the factor of two correction for the nebula field is not applied. Faded grey points correspond to null or low paleointensities, which may be due to formation of magnetite by pseudomorphic replacement which cannot record a chemical remnant magnetisation (CRM) (Bryson et al., 2023). The blue circles indicate pre-accretionary remanences from chondrules. The IVA irons have not been included, because they were generated by a solidifying, unmantled core (Bryson et al., 2017). The R chondrites have too large an age uncertainty and the CV chondrules are too altered to provide useful constraints so are not shown (Cournède et al., 2020; Shah et al., 2017). Intensity bars with arrows indicate values with a upper/lower limit (the cap) and for the CV_{ox,A} the best guess is the intersection with the time error bar. Our new model brings forward the onset of dynamo generation (pink box) relative to previous models (blue box). The orange box indicates the duration of the nebula field, which may be 1 Ma longer than shown here if the angrite age is recalculated based on Piralla et al. (2023). This would further increase the overlap between dynamo and nebula fields. The maximum paleointensity for a given planetesimal radius is shown by the graduated shading in the blue and pink regions. Data and references for this table are given in the Supplementary Materials.

However, in Kaba and the CO chondrites, magnetite formed by pseudomorphic replacement during aqueous alteration, which may be unable to record a remanence (Bryson et al., 2023). As a result, these null measurements may not indicate the absence of the nebula field. Tagish lake is also unmagnetised, but this has been attributed to its distal Solar System formation rather than the absence of a nebula field (Bryson et al., 2020b).

4.1.2. Ambiguous paleomagnetic records: nebula or dynamo fields?

Interpretation of bulk chondrite paleomagnetic remanences from the first 5 Ma after CAI formation is complicated by the possibility that these meteorites could sample the outer layers of a partially differentiated planetesimal (Carpözen et al., 2011; Elkins-Tanton et al., 2011; Weiss and Elkins-Tanton, 2013). Previously there were two possibilities for these remanences both of which were interpreted as evidence for a nebula field. First, the parent body was undifferentiated. Second, the parent body was partially differentiated, but dynamo onset was delayed by core thermal stratification (Dodds et al., 2021). However, we have shown in this work there is a third possibility: a partially differentiated parent body with $^{60}\text{Fe}/^{56}\text{Fe} \geq 10^{-8}$ would have an early onset of a thermal dynamo. Therefore, demonstrating that a remanence was acquired early is no longer sufficient to differentiate between dynamo and nebula fields. This could alter the interpretation of remanences in the CM and CV chondrites and WIS 91600 (green points in Figure 7). The R chondrites have too poorly constrained ages from 0–20 Myr after CAI formation (Cournède et al., 2020) to be discussed.

The matrix of CM chondrites records a unidirectional chemical remnant magnetisation (CRM) from aqueous alteration 2–4 Ma after CAI formation (Cournède et al., 2015; Bryson et al., 2023). There are two contrasting paleointensity measurements of $4 \pm 3 \mu\text{T}$ (Cournède et al., 2015) and $31 \pm 17 \mu\text{T}$ (Bryson et al., 2023). However, correcting for the apparent inefficiency of CRM acquisition by magnetite formed by pseudomorphic replacement and the relative amounts of pyrrhotite in these samples suggests all CM chondrites experienced a nebula field of $\sim 78 \mu\text{T}$ (Bryson et al., 2023). These remanences have previously been attributed to the nebula field due to their timing and lack of evidence for any prolonged thermal metamorphism (peak temperatures $< 100^\circ\text{C}$ Suttle et al., 2021).

WIS 91600 records a $4.4 \pm 2.2 \mu\text{T}$ TRM (Bryson et al., 2020a). The cooling rate of WIS 91600 is on the order of hours, suggesting this meteorite was heated transiently by an impact. The impact fields were too short-lived to be recorded hence the magnetic remanence was either caused by the nebula field or a dynamo field. WIS 91600 has not been dated directly but comparison with other impacted aqueously altered meteorites suggest this remanence was recorded 3.6–5 Ma after CAI formation (Bryson et al., 2020a). As with the CM chondrites, the old age and the absence of evidence of prolonged heating were used as evidence for WIS 91600 recording a nebula field.

For both the CM chondrites and WIS 91600, we have shown dynamo fields could have been generated during the time they recorded a remanence. The low peak temperatures of these meteorites could be because they sample the topmost layer of a partially differentiated body. Further numerical modelling of partially differentiated bodies combining gradual accretion and ^{60}Fe are required to determine if this is a viable possibility.

The CV chondrites experienced prolonged thermal metamorphism and bulk medium temperature magnetic remanences in Allende suggest the presence of a dynamo 5–40 Ma after CAI formation on a partially differentiated planetesimal (Carpözen et al., 2011; Elkins-Tanton et al., 2011; Gattacceca et al., 2016). The attribution of earlier

remanences to a nebula or dynamo field is debated and is complicated by the alteration of CV chondrules by impacts, heating and aqueous alteration (Fu et al., 2014a; Shah et al., 2017). Randomly oriented magnetisations between subsamples of the same chondrule indicate that CV chondrules do not record a pre-accretionary nebula field (Fu et al., 2014a; Shah et al., 2017). A more recent study found a medium temperature remanence in iron sulfides and not in the FeNi minerals in the Allende matrix suggesting Allende records a CRM from aqueous alteration 2.5–3.5 Ma after CAI formation (Fu et al., 2021). This remanence was interpreted as evidence for the nebula field based on the timing (Fu et al., 2021) and the lack of a high temperature magnetisation in CV chondrite Kaba aqueously altered shortly after (4–6 Ma after CAI formation Gattacceca et al., 2016; Weiss et al., 2021). However, the magnetite in Kaba formed by pseudomorphic replacement so was unable to record a CRM rather than a field being absent (Bryson et al., 2023). Since the Kaba null CRM no longer precludes the presence of a magnetic field 4–6 Ma after CAI formation, the uniform remanence in CV chondrites could be an early dynamo caused by ^{60}Fe .

Next, we assess whether paleointensity can be used to determine if a remanence has a dynamo or nebula field origin. As shown in Figure 7, the maximum nebula intensities measured are stronger than the maximum intensities predicted by our dynamo model. However, the quoted nebula intensities recorded by Winchcombe (CM, Bryson et al., 2023) and CV chondrites (Fu et al., 2021) are a factor of two larger than the measured paleointensities to account for rotation of the parent body during remanence acquisition. If these paleointensities were produced by dynamo fields this correction would not be required, which brings them within the range of field strengths predicted by our dynamo models (dashed lines on Figure 7). Our upper limits on dynamo field strengths ($> 30 \mu\text{T}$) are for the largest planetesimals with highest values of ^{60}Fe . Most parameter combinations predict lower dynamo strengths at early times (10–30 μT , Figure 3 and S1–S4). If the uncertainty on the paleointensity measurements can be reduced and parent body size and $^{60}\text{Fe}/^{56}\text{Fe}$ can be independently constrained, e.g. by thermal models and isotopic measurements, then even without the factor of two amplification measured paleointensities may be too strong to be dynamo generated. Regardless of improved measurements, the difficulty in converting an ARM to a TRM or TRM to CRM, which has correction factors of 2–5 (Weiss and Tikoo, 2014) and uncertainties in the ratio of dipole field at the CMB to the internal dynamo field from dynamo scaling laws (0.06–0.1 for Earth, Davies et al., 2022) may mean that the uncertainties of measured and predicted paleointensities overlap. Overall, the recovered paleointensities currently cannot be used to distinguish between a dynamo or nebula field.

The possibility of the earlier onset of a thermal dynamo due ^{60}Fe reduces the number of meteorite paleomagnetic studies that provide compelling evidence for the nebula field in the outer Solar System, because the bulk remanences in CM and CV chondrites may not record nebula fields. This should be considered when using this data to discuss differences in field strength and protoplanetary disk dispersal time between the inner and outer Solar System (Weiss

et al., 2021; Borlina et al., 2022). Paleomagnetic measurements of individual, pristine chondrules are vital to understand the nebula field, because their directions can indicate conclusively if a remanence is preaccretionary.

4.1.3. *Paleomagnetic constraints on primordial $^{60}\text{Fe}/^{56}\text{Fe}$*

The null paleointensities in the volcanic angrites and NWA 7325 at 3.8–5 Ma after CAI formation contradicts the early onset of a dynamo in bodies with $^{60}\text{Fe}/^{56}\text{Fe} \geq 10^{-8}$ predicted by this model. Magnetic remanences in the plutonic angrite, Angra dos Reis at 11 Ma after CAI formation (Wang et al., 2017) indicate the angrite parent body was differentiated and did generate a dynamo later in its history. Explanations, such as parent body size, gradual accretion and ^{60}Fe fractionation, are unlikely to cause this delay in dynamo onset (see Supplementary Materials). Another explanation could be $^{60}\text{Fe}/^{56}\text{Fe}$ was $\leq 10^{-9}$ in the formation region of the angrites and the time taken to erode core thermal stratification led to a delay in dynamo generation (Bryson et al., 2019a; Dodds et al., 2021). Tang and Dauphas (2012) measured values of $^{60}\text{Fe}/^{56}\text{Fe} = 0.9 \pm 0.5 \times 10^{-8}$ in the angrites. Additionally, values of $^{60}\text{Fe}/^{56}\text{Fe}$ from silicates in non-carbonaceous chondrules are within error of zero ($0.8 \pm 1.0 \times 10^{-7}$, Kodolányi et al., 2022a). For a 300 km body accreted at 0.8 Ma after CAI formation $^{60}\text{Fe}/^{56}\text{Fe} < 1.75 \times 10^{-9}$ gives a dynamo onset time consistent with the angrite data (see Figure S5). This limit lies within the lower bounds of these non-carbonaceous $^{60}\text{Fe}/^{56}\text{Fe}$ values. Current measurements from the carbonaceous IID and IVB irons ($6 \pm 2 \times 10^{-7}$, Cook et al., 2021) and carbonaceous chondrule silicates ($4 \pm 2 \times 10^{-7}$ Kodolányi et al., 2022a) have large uncertainties, but neither are within error of $^{60}\text{Fe}/^{56}\text{Fe} < 10^{-8}$. This suggests there could be heterogeneity in $^{60}\text{Fe}/^{56}\text{Fe}$ between the carbonaceous and non-carbonaceous reservoirs (Cook et al., 2021; Kodolányi et al., 2022a). Measurement of a paleomagnetic remanence in a carbonaceous achondrite between the age of the volcanic and plutonic angrites could provide evidence for this heterogeneity. If such a carbonaceous achondrite has a null paleomagnetic remanence, this could provide evidence for $^{60}\text{Fe}/^{56}\text{Fe} < 10^{-8}$ throughout the Solar System and constrain the timing of the dissipation of the nebula field in the outer Solar System. If a carbonaceous achondrite is found to have acquired a remanence at a similar time that the volcanic angrites did not (i.e., when the nebula field has dissipated), this could provide evidence for early dynamo onset and heterogeneity in $^{60}\text{Fe}/^{56}\text{Fe}$ in the early Solar System.

4.1.4. *Paleomagnetic records of planetesimal core crystallisation*

Our results argue that young remanences (> 65 Ma after CAI formation based on the current meteorite record) do not require the presence of a solidifying core. The first epoch of dynamo generation can last until 20–200 Ma after CAI formation (depending on radius) rather than until 9–34 Ma after CAI formation suggested by previous models (Dodds et al., 2021). Additionally, our improved core solidification model has revealed the second epoch of dynamo generation can begin prior to the onset of core solidification. As a result, the source of buoyancy to drive a dynamo cannot be assumed purely based on timing of a magnetic remanence. For extremes of some parameter values (low

η_0 and $X_{S,0}$), onset of solidification is early and most of dynamo generation is powered by a combination of thermal and compositional buoyancy. Previous studies on the Main Group pallasites (Bryson et al., 2015; Nichols et al., 2021) and IIE irons (Maurel et al., 2020) have used the onset of the late-stage dynamo as an indicator for the start of core solidification. This assumption has been used to constrain planetesimal radius, core size, thermal history and core composition. Our model highlights that the beginning of a second epoch of dynamo is unlikely to be coincident with core solidification, and therefore these studies must be re-evaluated.

4.2. Recommendations for future planetesimal thermal evolution models

A range of ^{60}Fe should be included in future thermal evolution models until the concentration and spatial distribution within the disk are better constrained. While the fractional increase in core temperature due to ^{60}Fe is small (9 K increase in peak temperature for $^{60}\text{Fe}/^{56}\text{Fe} = 6 \times 10^{-7}$ compared to $^{60}\text{Fe}/^{56}\text{Fe} = 0$), the increase in core temperature relative to the core-mantle temperature difference is large. This increased temperature has two significant effects on dynamo generation: early dynamo onset and increased dynamo strength. The possibility of these high $^{60}\text{Fe}/^{56}\text{Fe}$ values must be included in future thermal evolution models.

A lower, more realistic value of the mantle critical melt fraction, ϕ_C , based on experiments (0.25 – 0.3, Scott and Kohlstedt, 2006) should be used in future models to avoid overestimating the magnetic field strength, dynamo duration, and planetesimal peak temperature (see Appendix B). Due to the uncertainties in measured paleointensities the effect of ϕ_C on planetesimal peak temperature is the most important. This recommendation extends beyond 1D single-phase thermal evolution and dynamo models presented here to two-phase flow models, where $\phi_C = 0.5$ is often taken as the onset of a magma ocean and convection (e.g. Lichtenberg et al., 2019; Monnereau et al., 2023). These two-phase flow models are used to model differentiation and overestimating planetesimal peak temperatures may alter the Fe-FeS compositions that can be molten and the time available for processes such as percolation prior to the onset of a magma ocean.

Results from thermal evolution models need to account for variation in mantle reference viscosity, η_0 , as well as radius, when predicting timings of dynamo generation. The value of η_0 has a strong effect on the duration of the gap between dynamo generation epochs and the onset of core solidification, but is poorly constrained. The extrapolated range of η_0 values runs across the threshold value for a gap in dynamo generation, which occurs for $\eta_0 > 10^{16}$ Pas. Therefore, as a minimum, future thermal evolution models should include runs for one η_0 value above and below the threshold when attempting to recreate a parent body thermal history. Future models could attempt to constrain values for η_0 (and other viscosity parameters) based on parent body composition, water content and observed gaps in the paleomagnetic record.

4.3. Validity

This work only explored variations within one parameter at a time, while all other parameters were held at their median value. Using endmember values for multiple parameters simultaneously may result in an even wider range of dynamo generation times. Varying a single parameter enables the effect of each parameter to be understood and the dominant factors in dynamo generation timing to be isolated. As demonstrated in Figure 5, even across variations in parameters other than radius, there are large portions of time where the planetesimal dynamo is consistently active. Therefore, even if multiple parameters are varied, the trends in timing with radius predicted here are likely to hold true. The choice of critical Re_m , $X_{S,0}$, and assumptions about accretion and differentiation are justified for the purposes of this work and do not have a large impact on the results (for further discussion see the Supplementary Materials).

5. Conclusions

Using the refined planetesimal thermal evolution model of Sanderson et al. (2024), we explored the effects of ^{60}Fe , mantle viscosity, initial core sulfur content and planetesimal radius on planetesimal dynamo generation. Our results suggest there is a wider range in dynamo timings and durations than previously predicted. The meteorite paleomagnetic record cannot be split into three distinct epochs of magnetic field generation and the implications of some paleomagnetic remanences should be re-evaluated.

- Inclusion of ^{60}Fe in the core can bring forward the onset of thermal dynamos to 1–2 Ma after CAI formation, extending the time at which the first planetesimal dynamos were possible. Some meteorite remanences recorded prior to 5 Ma after CAI formation could have a dynamo rather than nebula field origin.
- Null paleomagnetic remanences in the angrites contradict the early onset of thermal dynamos from ^{60}Fe . This could provide evidence for heterogeneous $^{60}\text{Fe}/^{56}\text{Fe}$ in the early Solar System. Paleomagnetic measurements of an old (<10 Ma after CAI formation) carbonaceous achondrite could help confirm this.
- Planetesimal radius strongly affects the start time of the gap in planetesimal dynamo generation (20–200 Ma after CAI formation) and final end of dynamo duration (40–640 Ma after CAI formation).
- The paleomagnetic record does not reflect early thermal dynamos and later compositional dynamos, as previously interpreted. Variation in initial core sulfur content and mantle reference viscosity can produce early thermo-compositional dynamos. For most parameter combinations, there is a second thermal dynamo period prior to the onset of core solidification.

- Young magnetic remanences (>65 Ma post CAI formation based on the current record) do not require a solidifying core. As a result, the planetesimal radii, core sizes, thermal histories and core compositions of the Main Group pallasites and IIE irons need reevaluating.
- A range of radii, reference viscosities, $^{60}\text{Fe}/^{56}\text{Fe}$ should be explored when attempting to constrain parent body properties based on a magnetic remanence.

CRediT authorship contribution statement

Hannah R. Sanderson: Conceptualization, Methodology, Software, Writing - Original Draft. **James F.J. Bryson:** Conceptualization, Writing - Review & Editing, Supervision. **Claire I.O. Nichols:** Conceptualization, Writing - Review & Editing, Supervision.

Declaration of competing interest

The authors declare that they have no known competing financial interests or personal relationships that could have appeared to influence the work reported in this paper.

Data availability

The dynamo and thermal evolution model and the parameter files required to recreate the results in this paper are publicly available the Sanderson (2024) Github repository.

Acknowledgements

The authors would like to thank Kathryn Dodds and Chris Davies for their helpful discussions in preparing this work. HS acknowledges funding on a NERC studentship NE/S007474/1 and an Exonian Graduate Scholarship from Exeter College, University of Oxford. HRS thanks the Royal Astronomical Society for a student travel grant that enabled this work to be presented at the American Geophysical Union Fall Meeting 2023. JFJB acknowledges funding from the UKRI Research Frontier Guarantee program EP/Y014375/1. For the purpose of open access, the authors have applied a Creative Commons Attribution (CC BY) licence to any Author Accepted Manuscript version arising.

A. Extrapolation of reference viscosities

Viscosity is temperature and pressure dependent. Planetesimal mid-mantle pressures lie above that of lab experiments and below that of planets, therefore extrapolation is required when estimating planetesimal reference viscosities. Laboratory experiments are also on shorter timescales and lengthscales compared to planetary conditions.

η_0 /Pas	p_{ref} /MPa	T_{ref} /K	Extrapolated η_0 /Pas
10^{19} – 10^{22}	960	1600	10^{19} – 10^{24}

Table 2

Reference parameters for viscosity extrapolations for Ganymede (Rückriemen et al., 2018). Reference pressure is calculated in the mid-mantle using average values for the Ganymede interior structure model in Rückriemen et al. (2018).

Therefore, geophysical observations, such as postglacial uplift (Karato and Wu, 1993) are often used to constrain mantle viscosity on Earth. For this reason, the full range of η_0 in this paper was extrapolated from planetary values and the experimental values were included as a lower bound. Extrapolation can be done using an Arrhenius law

$$\eta = \eta_0 \exp \left(\frac{E + pV}{RT} - \frac{E + p_{ref}V}{RT_{ref}} \right) \quad (1)$$

or the Frank-Kamenetskii approximation (Noack and Breuer, 2013)

$$\eta = \eta_0 \exp \left(\frac{E + p_{ref}V}{RT_{ref}^2} (T_{ref} - T) + \frac{V}{RT_{ref}} (p - p_{ref}) \right). \quad (2)$$

In these equations, E and V are the activation energy and volume, p_{ref} and T_{ref} are the reference pressures and temperatures, R is the gas constant and p and T are the temperatures and pressures being extrapolated to. To estimate planetesimal mid-mantle viscosities extrapolations using both laws were performed on reference viscosity values for Ganymede (Rückriemen et al., 2018) (see Table 2) using a range in activation volumes from 2×10^{-6} – 2×10^{-5} m³mol⁻¹ (Hirth and Kohlstedt, 2003) and activation energies from 240–570 kJmol⁻¹ (Karato and Wu, 1993; Hirth and Kohlstedt, 2003). Assuming constant density core and mantle, planetesimal mid-mantle pressures range from 2 MPa to 50 MPa for 100–500 km bodies. These extrapolations give possible a wide range η_0 from 10^{19} – 10^{24} Pas due to the large uncertainties in activation volume and activation energy. Equation 1 and 2 give values within the same order of magnitude.

B. Effect of ϕ_C on peak temperatures

As shown in Figure 8, peak mantle temperature is close to that of ϕ_C due to the negative feedback loop between mantle temperature and stagnant lid thickness. At ϕ_C , an increase in temperature leads to a rapid drop in viscosity and thinning of the stagnant lid. This increases surface heat flux, which reduces mantle temperature, increases the viscosity and thickens the stagnant lid. This means choice of ϕ_C has direct control on the maximum mantle temperature of a planetesimal.

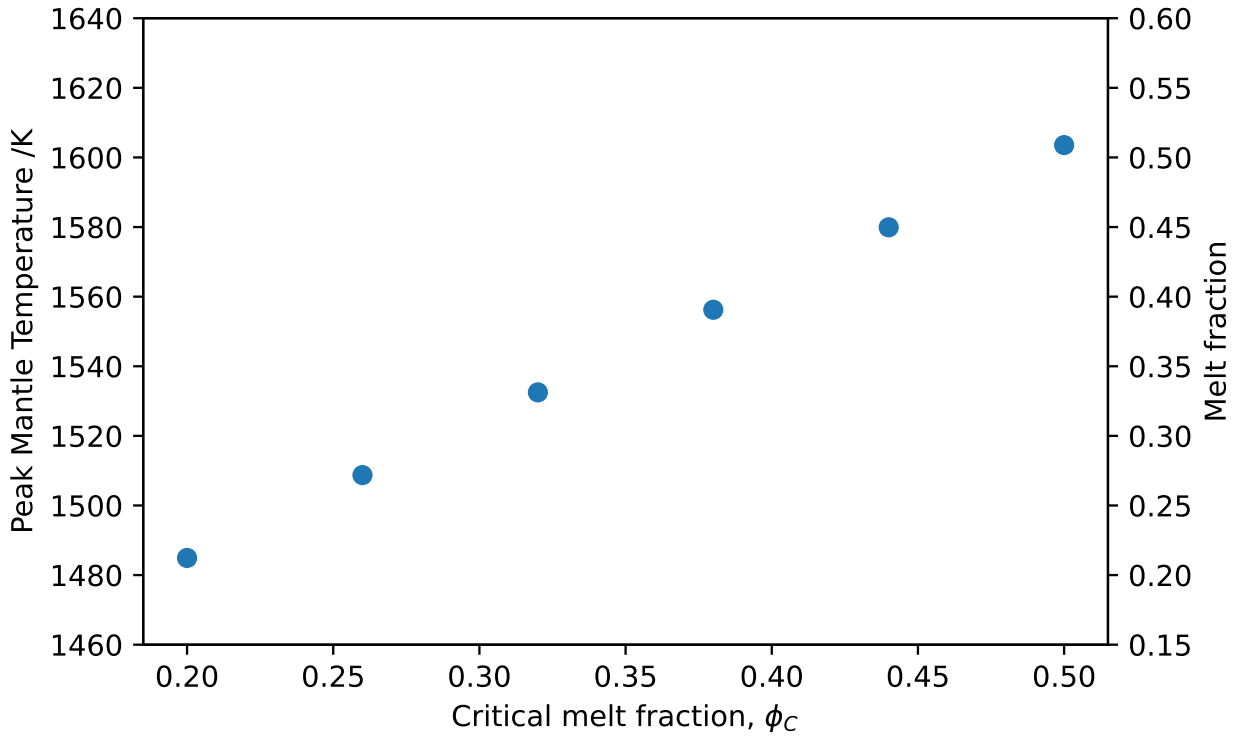


Figure 8: Peak mantle temperature as a function of ϕ_C .

References

- Aubert, J., Labrosse, S., Poitou, C., 2009. Modelling the palaeo-evolution of the geodynamo. *Geophysical Journal International* 179, 1414–1428. URL: <https://academic.oup.com/gji/article/179/3/1414/775893>, doi:10.1111/J.1365-246X.2009.04361.X/3/179-3-1414-FIG012.JPEG. publisher: Oxford Academic.
- Borlina, C.S., Weiss, B.P., Bryson, J.F.J., Armitage, P.J., 2022. Lifetime of the Outer Solar System Nebula From Carbonaceous Chondrites. *Journal of Geophysical Research: Planets* 127, e2021JE007139. URL: <https://onlinelibrary.wiley.com/doi/abs/10.1029/2021JE007139>, doi:10.1029/2021JE007139. _eprint: <https://onlinelibrary.wiley.com/doi/pdf/10.1029/2021JE007139>.
- Borlina, C.S., Weiss, B.P., Bryson, J.F.J., Bai, X.N., Lima, E.A., Chatterjee, N., Mansbach, E.N., 2021. Paleomagnetic evidence for a disk substructure in the early solar system. *Science Advances* 7, eabj6928. URL: <https://www.science.org/doi/full/10.1126/sciadv.abj6928>, doi:10.1126/sciadv.abj6928. publisher: American Association for the Advancement of Science.
- Bryson, J.F., Neufeld, J.A., Nimmo, F., 2019a. Constraints on asteroid magnetic field evolution and the radii of meteorite parent bodies from thermal modelling. *Earth and Planetary Science Letters* 521, 68–78. URL: <https://doi.org/10.1016/j.epsl.2019.05.046>, doi:10.1016/J.EPSL.2019.05.046. publisher: Elsevier B.V.
- Bryson, J.F., Nichols, C.I., Herrero-Albillos, J., Kronast, F., Kasama, T., Alimadadi, H., Van Der Laan, G., Nimmo, F., Harrison, R.J., 2015. Long-lived magnetism from solidification-driven convection on the pallasite parent body. *Nature* 517:7535–7540, 472–475. URL: <https://www.nature.com/articles/nature14114>, doi:10.1038/nature14114. publisher: Nature Publishing Group.

- Bryson, J.F.J., Nichols, C.I.O., Mac Niocaill, C., 2023. A unified intensity of the magnetic field in the protoplanetary disk from the Winchcombe meteorite. *Meteoritics & Planetary Science* n/a, 1–22. URL: <https://onlinelibrary.wiley.com/doi/abs/10.1111/maps.14079>, doi:10.1111/maps.14079. _eprint: <https://onlinelibrary.wiley.com/doi/pdf/10.1111/maps.14079>.
- Bryson, J.F.J., Weiss, B.P., Biersteker, J.B., King, A.J., Russell, S.S., 2020a. Constraints on the Distances and Timescales of Solid Migration in the Early Solar System from Meteorite Magnetism. *The Astrophysical Journal* 896, 103. URL: <https://dx.doi.org/10.3847/1538-4357/ab91ab>, doi:10.3847/1538-4357/ab91ab. publisher: The American Astronomical Society.
- Bryson, J.F.J., Weiss, B.P., Getzin, B., Abrahams, J.N.H., Nimmo, F., Scholl, A., 2019b. Paleomagnetic Evidence for a Partially Differentiated Ordinary Chondrite Parent Asteroid. *Journal of Geophysical Research: Planets* 124, 1880–1898. URL: <https://onlinelibrary.wiley.com/doi/abs/10.1029/2019JE005951>, doi:10.1029/2019JE005951. _eprint: <https://onlinelibrary.wiley.com/doi/pdf/10.1029/2019JE005951>.
- Bryson, J.F.J., Weiss, B.P., Harrison, R.J., Herrero-Albillos, J., Kronast, F., 2017. Paleomagnetic evidence for dynamo activity driven by inward crystallisation of a metallic asteroid. *Earth and Planetary Science Letters* 472, 152–163. URL: <https://www.sciencedirect.com/science/article/pii/S0012821X17302923>, doi:10.1016/j.epsl.2017.05.026.
- Bryson, J.F.J., Weiss, B.P., Lima, E.A., Gattacceca, J., Cassata, W.S., 2020b. Evidence for Asteroid Scattering and Distal Solar System Solids From Meteorite Paleomagnetism. *The Astrophysical Journal* 892, 126. URL: <https://dx.doi.org/10.3847/1538-4357/ab7cd4>, doi:10.3847/1538-4357/ab7cd4. publisher: The American Astronomical Society.
- Carporzen, L., Weiss, B.P., Elkins-Tanton, L.T., Shuster, D.L., Ebel, D., Gattacceca, J., 2011. Magnetic evidence for a partially differentiated carbonaceous chondrite parent body. *Proceedings of the National Academy of Sciences* 108, 6386–6389. URL: <https://www.pnas.org/doi/abs/10.1073/pnas.1017165108>, doi:10.1073/pnas.1017165108. publisher: Proceedings of the National Academy of Sciences.
- Christensen, U.R., Aubert, J., 2006. Scaling properties of convection-driven dynamos in rotating spherical shells and application to planetary magnetic fields. *Geophysical Journal International* 166, 97–114. URL: <https://doi.org/10.1111/j.1365-246X.2006.03009.x>, doi:10.1111/j.1365-246X.2006.03009.x.
- Cook, D.L., Meyer, B.S., Schönbächler, M., 2021. Iron and Nickel Isotopes in IID and IVB Iron Meteorites: Evidence for Admixture of an SN II Component and Implications for the Initial Abundance of ^{60}Fe . *The Astrophysical Journal* 917, 59. URL: <https://dx.doi.org/10.3847/1538-4357/ac0add>, doi:10.3847/1538-4357/ac0add. publisher: The American Astronomical Society.
- Cournède, C., Gattacceca, J., Gounelle, M., Rochette, P., Weiss, B.P., Zanda, B., 2015. An early solar system magnetic field recorded in CM chondrites. *Earth and Planetary Science Letters* 410, 62–74. URL: <https://www.sciencedirect.com/science/article/pii/S0012821X14007110>, doi:10.1016/j.epsl.2014.11.019.
- Cournède, C., Gattacceca, J., Rochette, P., Shuster, D.L., 2020. Paleomagnetism of Rumuruti chondrites suggests a partially differentiated parent body. *Earth and Planetary Science Letters* 533, 116042. URL: <https://www.sciencedirect.com/science/article/pii/S0012821X1930737X>, doi:10.1016/j.epsl.2019.116042.
- Davies, C.J., Bono, R.K., Meduri, D.G., Aubert, J., Greenwood, S., Biggin, A.J., 2022. Dynamo constraints on the long-term evolution of Earth’s magnetic field strength. *Geophysical Journal International* 228, 316–336. URL: <https://doi.org/10.1093/gji/ggab342>, doi:10.1093/gji/ggab342.
- Dodds, K.H., Bryson, J.F., Neufeld, J.A., Harrison, R.J., 2021. The Thermal Evolution of Planetesimals During Accretion and Differentiation: Consequences for Dynamo Generation by Thermally-Driven Convection. *Journal of Geophysical Research: Planets* 126. doi:10.1029/2020JE006704. publisher: Blackwell Publishing Ltd.
- Elkins-Tanton, L.T., Weiss, B.P., Zuber, M.T., 2011. Chondrites as samples of differentiated planetesimals. *Earth and Planetary Science Letters* 305, 1–10. URL: <https://www.sciencedirect.com/science/article/pii/S0012821X11001543>, doi:10.1016/j.epsl.2011.03.010.

- Fu, R.R., Kehayias, P., Weiss, B.P., Schrader, D.L., Bai, X.N., Simon, J.B., 2020. Weak Magnetic Fields in the Outer Solar Nebula Recorded in CR Chondrites. *Journal of Geophysical Research: Planets* 125, e2019JE006260. URL: <https://onlinelibrary.wiley.com/doi/abs/10.1029/2019JE006260>, doi:10.1029/2019JE006260. _eprint: <https://onlinelibrary.wiley.com/doi/pdf/10.1029/2019JE006260>.
- Fu, R.R., Lima, E.A., Weiss, B.P., 2014a. No nebular magnetization in the Allende CV carbonaceous chondrite. *Earth and Planetary Science Letters* 404, 54–66. URL: <https://www.sciencedirect.com/science/article/pii/S0012821X14004646>, doi:10.1016/j.epsl.2014.07.014.
- Fu, R.R., Volk, M.W.R., Bilardello, D., Libourel, G., Lesur, G.R.J., Dor, O.B., 2021. The Fine-Scale Magnetic History of the Allende Meteorite: Implications for the Structure of the Solar Nebula. *AGU Advances* 2, e2021AV000486. URL: <https://onlinelibrary.wiley.com/doi/full/10.1029/2021AV000486>, doi:10.1029/2021AV000486. publisher: John Wiley & Sons, Ltd ISBN: 10.1029/2021.
- Fu, R.R., Weiss, B.P., Lima, E.A., Harrison, R.J., Bai, X.N., Desch, S.J., Ebel, D.S., Suavet, C., Wang, H., Glenn, D., Le Sage, D., Kasama, T., Walsworth, R.L., Kuan, A.T., 2014b. Solar nebula magnetic fields recorded in the Semarkona meteorite. *Science* 346, 1089–1092. URL: <https://www.science.org/doi/10.1126/science.1258022>, doi:10.1126/science.1258022. publisher: American Association for the Advancement of Science.
- Gattacceca, J., Weiss, B.P., Gounelle, M., 2016. New constraints on the magnetic history of the CV parent body and the solar nebula from the Kaba meteorite. *Earth and Planetary Science Letters* 455, 166–175. URL: <https://www.sciencedirect.com/science/article/pii/S0012821X16304885>, doi:10.1016/j.epsl.2016.09.008.
- Giordano, D., Russell, J.K., Dingwell, D.B., 2008. Viscosity of magmatic liquids: A model. *Earth and Planetary Science Letters* 271, 123–134. URL: <https://www.sciencedirect.com/science/article/pii/S0012821X08002240>, doi:10.1016/j.epsl.2008.03.038.
- Henke, S., Gail, H.P., Trieloff, M., Schwarz, W.H., 2013. Thermal evolution model for the H chondrite asteroid-instantaneous formation versus protracted accretion. *Icarus* 226, 212–228. URL: <http://dx.doi.org/10.1016/j.icarus.2013.05.034>, doi:10.1016/J.ICARUS.2013.05.034.
- Hirth, G., Kohlstedt, D., 2003. Rheology of the Upper Mantle and the Mantle Wedge: A View from the Experimentalists, in: *Inside the Subduction Factory*. American Geophysical Union. volume 138 of *Geophysical Monograph Series*, pp. 83–105. URL: 10.1029/GM138. doi:10.1029/138GM06.
- Karato, S.i., Wu, P., 1993. Rheology of the Upper Mantle: A Synthesis. *Science* 260, 771–778. URL: <https://www.science.org/doi/10.1126/science.260.5109.771>, doi:10.1126/science.260.5109.771. publisher: American Association for the Advancement of Science.
- Kodolányi, J., Hoppe, P., Vollmer, C., Berndt, J., Müller, M., 2022a. The Early Solar System Abundance of Iron-60: New Constraints from Chondritic Silicates. *The Astrophysical Journal* 940, 95. URL: <https://dx.doi.org/10.3847/1538-4357/ac8b85>, doi:10.3847/1538-4357/ac8b85. publisher: The American Astronomical Society.
- Kodolányi, J., Hoppe, P., Vollmer, C., Berndt, J., Müller, M., 2022b. Iron-60 in the Early Solar System Revisited: Insights from In Situ Isotope Analysis of Chondritic Troilite. *The Astrophysical Journal* 929, 107. URL: <https://dx.doi.org/10.3847/1538-4357/ac5910>, doi:10.3847/1538-4357/ac5910. publisher: The American Astronomical Society.
- Leshner, C.E., Spera, F.J., 2015. Chapter 5 - Thermodynamic and Transport Properties of Silicate Melts and Magma, in: Sigurdsson, H. (Ed.), *The Encyclopedia of Volcanoes (Second Edition)*. Academic Press, Amsterdam, pp. 113–141. URL: <https://www.sciencedirect.com/science/article/pii/B9780123859389000055>, doi:10.1016/B978-0-12-385938-9.00005-5.
- Lichtenberg, T., Keller, T., Katz, R.F., Golabek, G.J., Gerya, T.V., 2019. Magma ascent in planetesimals: Control by grain size. *Earth and Planetary Science Letters* 507, 154–165. doi:10.1016/J.EPSL.2018.11.034. arXiv: 1802.02157 Publisher: Elsevier.
- Maurel, C., Bryson, J.F.J., Lyons, R.J., Ball, M.R., Chopdekar, R.V., Scholl, A., Ciesla, F.J., Bottke, W.F., Weiss, B.P., 2020. Meteorite evidence for partial differentiation and protracted accretion of planetesimals. *Science Advances* 6, eaba1303. URL: <https://www.science.org/doi/10.1126/sciadv.aba1303>, doi:10.1126/sciadv.aba1303. publisher: American Association for the Advancement of Science.

- Maurel, C., Bryson, J.F.J., Shah, J., Chopdekar, R.V., T. Elkins-Tanton, L., A. Raymond, C., Weiss, B.P., 2021. A Long-Lived Planetary Dynamo Powered by Core Crystallization. *Geophysical Research Letters* 48, e2020GL091917. URL: <https://onlinelibrary.wiley.com/doi/abs/10.1029/2020GL091917>, doi:10.1029/2020GL091917. eprint: <https://onlinelibrary.wiley.com/doi/pdf/10.1029/2020GL091917>.
- Maurel, C., Gattacceca, J., 2024. A 4,565-My-old record of the solar nebula field. *Proceedings of the National Academy of Sciences* 121, e2312802121. URL: <https://www.pnas.org/doi/10.1073/pnas.2312802121>, doi:10.1073/pnas.2312802121. publisher: Proceedings of the National Academy of Sciences.
- Monnereau, M., Guignard, J., Néri, A., Toplis, M.J., Quitté, G., 2023. Differentiation time scales of small rocky bodies. *Icarus* 390, 115294. URL: <https://www.sciencedirect.com/science/article/pii/S0019103522003864>, doi:10.1016/j.icarus.2022.115294.
- Neufeld, J.A., Bryson, J.F., Nimmo, F., 2019. The Top-Down Solidification of Iron Asteroids Driving Dynamo Evolution. *Journal of Geophysical Research: Planets* 124, 1331–1356. URL: <https://onlinelibrary.wiley.com/doi/full/10.1029/2018JE005900>, doi:10.1029/2018JE005900. publisher: John Wiley & Sons, Ltd.
- Neumann, W., Luther, R., Trierloff, M., Reger, P.M., Bouvier, A., 2023. Fitting Thermal Evolution Models to the Chronological Record of Erg Chech 002 and Modeling the Ejection Conditions of the Meteorite. *The Planetary Science Journal* 4, 196. URL: <https://iopscience.iop.org/article/10.3847/PSJ/acf465/meta>, doi:10.3847/PSJ/acf465. publisher: IOP Publishing.
- Nichols, C.I., Bryson, J.F., Cottrell, R.D., Fu, R.R., Harrison, R.J., Herrero-Albillos, J., Kronast, F., Tarduno, J.A., Weiss, B.P., 2021. A Time-Resolved Paleomagnetic Record of Main Group Pallasites: Evidence for a Large-Cored, Thin-Mantled Parent Body. *Journal of Geophysical Research: Planets* 126, e2021JE006900. URL: <https://onlinelibrary.wiley.com/doi/full/10.1029/2021JE006900>, doi:10.1029/2021JE006900. publisher: John Wiley & Sons, Ltd ISBN: 10.1029/2021.
- Nichols, C.I., Bryson, J.F., Herrero-Albillos, J., Kronast, F., Nimmo, F., Harrison, R.J., 2016. Pallasite paleomagnetism: Quiescence of a core dynamo. *Earth and Planetary Science Letters* 441, 103–112. doi:10.1016/J.EPSL.2016.02.037. publisher: Elsevier.
- Nimmo, F., 2009. Energetics of asteroid dynamos and the role of compositional convection. *Geophysical Research Letters* 36. URL: <https://onlinelibrary.wiley.com/doi/full/10.1029/2009GL037997>, doi:10.1029/2009GL037997. publisher: John Wiley & Sons, Ltd.
- Noack, L., Breuer, D., 2013. First- and second-order Frank-Kamenetskii approximation applied to temperature-, pressure- and stress-dependent rheology. *Geophysical Journal International* 195, 27–46. URL: <https://doi.org/10.1093/gji/ggt248>, doi:10.1093/gji/ggt248.
- Oran, R., Weiss, B.P., Cohen, O., 2018. Were chondrites magnetized by the early solar wind? *Earth and Planetary Science Letters* 492, 222–231. URL: <https://www.sciencedirect.com/science/article/pii/S0012821X1830075X>, doi:10.1016/j.epsl.2018.02.013.
- O'Brien, T., Tarduno, J.A., Anand, A., Smirnov, A.V., Blackman, E.G., Carroll-Nellenback, J., Krot, A.N., 2020. Arrival and magnetization of carbonaceous chondrites in the asteroid belt before 4562 million years ago. *Communications Earth & Environment* 1, 1–7. URL: <https://www.nature.com/articles/s43247-020-00055-w>, doi:10.1038/s43247-020-00055-w. publisher: Nature Publishing Group.
- Piralla, M., Villeneuve, J., Schnuriger, N., Bekaert, D.V., Marrocchi, Y., 2023. A unified chronology of dust formation in the early solar system. *Icarus* 394, 115427. URL: <https://www.sciencedirect.com/science/article/pii/S0019103523000040>, doi:10.1016/j.icarus.2023.115427.
- Rückriemen, T., Breuer, D., Spohn, T., 2015. The Fe snow regime in Ganymede's core: A deep-seated dynamo below a stable snow zone. *Journal of Geophysical Research: Planets* 120, 1095–1118. URL: <https://onlinelibrary.wiley.com/doi/full/10.1002/2014JE004781>, doi:10.1002/2014JE004781. publisher: John Wiley & Sons, Ltd.
- Rückriemen, T., Breuer, D., Spohn, T., 2018. Top-down freezing in a Fe–FeS core and Ganymede's present-day magnetic field. *Icarus* 307, 172–196. URL: <https://www.sciencedirect.com/science/article/pii/S0019103517307029>, doi:10.1016/j.icarus.2018.02.021.
- Sanderson, H., 2024. A refined, versatile model for planetesimal thermal evolution and dynamo generation. URL: <https://github.com/Hannah-RS/planetesimal-magnetic-history>, doi:10.5281/zenodo.11147998.

- Sanderson, H., Bryson, J.F.J., Nichols, C.I.O., 2024. Unlocking planetesimal magnetic field histories: a refined, versatile model for thermal evolution and dynamo generation.
- Scheinberg, A., Elkins-Tanton, L.T., Schubert, G., Bercovici, D., 2016. Core solidification and dynamo evolution in a mantle-stripped planetesimal. *Journal of Geophysical Research: Planets* 121, 2–20. URL: <https://onlinelibrary.wiley.com/doi/full/10.1002/2015JE004843>, doi:10.1002/2015JE004843. publisher: John Wiley & Sons, Ltd.
- Scott, T., Kohlstedt, D.L., 2006. The effect of large melt fraction on the deformation behavior of peridotite. *Earth and Planetary Science Letters* 246, 177–187. doi:10.1016/J.EPSL.2006.04.027.
- Shah, J., Bates, H.C., Muxworthy, A.R., Hezel, D.C., Russell, S.S., Genge, M.J., 2017. Long-lived magnetism on chondrite parent bodies. *Earth and Planetary Science Letters* 475, 106–118. URL: <https://www.sciencedirect.com/science/article/pii/S0012821X17304193>, doi:10.1016/j.epsl.2017.07.035.
- Sterenborg, M.G., Crowley, J.W., 2012. Thermal evolution of early solar system planetesimals and the possibility of sustained dynamos. *Physics of the Earth and Planetary Interiors* URL: <http://dx.doi.org/10.1016/j.pepi.2012.10.006>, doi:10.1016/j.pepi.2012.10.006.
- Stevenson, D.J., 2003. Planetary magnetic fields. *Earth and Planetary Science Letters* 208, 1–11. URL: <https://www.sciencedirect.com/science/article/pii/S0012821X02011263>, doi:10.1016/S0012-821X(02)01126-3.
- Sturtz, C., Limare, A., Tait, S., Kaminski, E., 2022. Birth and Decline of Magma Oceans in Planetesimals: 2. Structure and Thermal History of Early Accreted Small Planetary Bodies. *Journal of Geophysical Research: Planets* 127, e2021JE007020. URL: <https://onlinelibrary.wiley.com/doi/abs/10.1029/2021JE007020>, doi:10.1029/2021JE007020. _eprint: <https://onlinelibrary.wiley.com/doi/pdf/10.1029/2021JE007020>.
- Suttle, M.D., King, A.J., Schofield, P.F., Bates, H., Russell, S.S., 2021. The aqueous alteration of CM chondrites, a review. *Geochimica et Cosmochimica Acta* 299, 219–256. URL: <https://www.sciencedirect.com/science/article/pii/S0016703721000363>, doi:10.1016/j.gca.2021.01.014.
- Tang, H., Dauphas, N., 2012. Abundance, distribution, and origin of ⁶⁰Fe in the solar protoplanetary disk. *Earth and Planetary Science Letters* 359–360, 248–263. URL: <https://www.sciencedirect.com/science/article/pii/S0012821X12005705>, doi:10.1016/j.epsl.2012.10.011.
- Tarduno, J.A., Cottrell, R.D., Nimmo, F., Hopkins, J., Voronov, J., Erickson, A., Blackman, E., Scott, E.R., McKinley, R., 2012. Evidence for a Dynamo in the Main Group Pallasite Parent Body. *Science* 338, 939–942. URL: <https://www.science.org/doi/full/10.1126/science.1223932>, doi:10.1126/science.1223932. publisher: American Association for the Advancement of Science.
- Tarduno, J.A., O'Brien, T.M., Blackman, E.G., Smirnov, A.V., 2017. Magnetization of CV Meteorites in the Absence of a Parent Body Core Dynamo, in: 48th Annual Lunar and Planetary Science Conference, p. 2850. URL: <https://ui.adsabs.harvard.edu/abs/2017LPI....48.2850T>.
- Wang, H., Weiss, B.P., Bai, X.N., Downey, B.G., Wang, J., Wang, J., Suavet, C., Fu, R.R., Zucolotto, M.E., 2017. Lifetime of the solar nebula constrained by meteorite paleomagnetism. *Science* 355, 623–627. URL: <https://www.science.org/doi/full/10.1126/science.aaf5043>, doi:10.1126/science.aaf5043. publisher: American Association for the Advancement of Science.
- Weiss, B.P., Bai, X.N., Fu, R.R., 2021. History of the solar nebula from meteorite paleomagnetism. *Science Advances* 7, eaba5967. URL: <https://www.science.org/doi/full/10.1126/sciadv.aba5967>, doi:10.1126/sciadv.aba5967. publisher: American Association for the Advancement of Science.
- Weiss, B.P., Elkins-Tanton, L.T., 2013. Differentiated Planetesimals and the Parent Bodies of Chondrites. *Annual Review of Earth and Planetary Sciences* 41, 529–560. URL: <https://doi.org/10.1146/annurev-earth-040610-133520>, doi:10.1146/annurev-earth-040610-133520. _eprint: <https://doi.org/10.1146/annurev-earth-040610-133520>.
- Weiss, B.P., Tikoo, S.M., 2014. The lunar dynamo. *Science* 346. URL: <https://www.science.org/doi/abs/10.1126/science.1246753>, doi:10.1126/SCIENCE.1246753/SUPPL_FILE/WEISS.SM.PDF. publisher: American Association for the Advancement of Science.

- Weiss, B.P., Wang, H., Sharp, T.G., Gattacceca, J., Shuster, D.L., Downey, B., Hu, J., Fu, R.R., Kuan, A.T., Suavet, C., Irving, A.J., Wang, J., Wang, J., 2017. A nonmagnetic differentiated early planetary body. *Earth and Planetary Science Letters* 468, 119–132. URL: <https://www.sciencedirect.com/science/article/pii/S0012821X17301620>, doi:10.1016/j.epsl.2017.03.026.
- Williams, Q., 2009. Bottom-up versus top-down solidification of the cores of small solar system bodies: Constraints on paradoxical cores. *Earth and Planetary Science Letters* 284, 564–569. doi:10.1016/J.EPSL.2009.05.019. publisher: Elsevier.